HHS Public Access

Author manuscript

*Neuron*. Author manuscript; available in PMC 2022 July 07.

Published in final edited form as:

*Neuron*. 2021 July 07; 109(13): 2131–2149.e15. doi:10.1016/j.neuron.2021.05.007.

# CIB2 and CIB3 are auxiliary subunits of the mechanotransduction channel of hair cells

**Xiaoping Liang**[1,*], **Xufeng Qiu**[1,*], **Gilman Dionne**[2,*], **Christopher L. Cunningham**[1], **Michele L. Pucak**[1], **Guihong Peng**[1], **Ye-Hyun Kim**[3], **Amanda Lauer**[3], **Lawrence Shapiro**[2], **Ulrich Müller**[1,#]

[1]The Solomon H. Snyder Department of Neuroscience, Johns Hopkins University School of Medicine, Baltimore, MD 21205, USA.

[2]Department of Biochemistry and Molecular Biophysics, Zuckerman Mind Brain, Department of Systems Biology, Columbia University, New York, NY 10032, USA.

[3]Department of Otolaryngology-HNS, Johns Hopkins University School of Medicine, Baltimore, MD 21205, USA.

## Summary

CIB2 is a $Ca^{2+}$- and $Mg^{2+}$-binding protein essential for mechanoelectrical transduction (MET) by cochlear hair cells but not by vestibular hair cells that co-express CIB2 and CIB3. Here we show that in cochlear hair cells CIB3 can functionally substitute for CIB2. Using X-ray crystallography, we demonstrate that CIB2 and CIB3 are structurally similar to KChIP proteins, auxiliary subunits of voltage-gated $K_V4$ channels. CIB2 and CIB3 bind to TMC1/2 through a domain in TMC1/2 flanked by transmembrane domains 2 and 3. The co-crystal structure of the CIB-binding domain in TMC1 with CIB3 reveals that interactions are mediated through a conserved CIB hydrophobic groove, similar to KChIP1 binding of $K_V4$. Functional studies in mice show that CIB2 regulates TMC1/2 localization and function in hair cells, processes that are affected by deafness-causing

Ulrich Müller, The Solomon H. Snyder Department of Neuroscience, Johns Hopkins University School of Medicine, Baltimore, MD 21205, USA. umuelle3@jhmi.edu, 443-287-4762.

*equal author contribution

#Lead contact

Author Contributions

XL carried out genetic, immunohistological, biochemical and structural experiments. XQ carried out genetic experiments, all electrophysiological recordings and immunolocalization studies. GD solved, refined, and analyzed the crystal structures and generated alignments for sequence analysis. CLC contributed to genetic experiments and immunolocalization studies. GP generated mutant mice and contributed to genetic experiments. XL, XQ, Y-HK and AL carried out ABR and DPOAE recordings. MP helped with imaging and image analysis. XL, XQ, GD, LS and UM designed the study. All authors contributed to data analysis. UM, GD, LS, XL and XQ wrote the manuscript.

Inclusion and Diversity

We worked to ensure sex balance in the selection of non-human subjects. The author list of this paper includes contributors from the location where the research was conducted who participated in the data collection, design, analysis, and/or interpretation of the work.

Declaration of Interests

Dr. Mueller is a co-founder of Decibel Therapeutics.

CIB2 mutations. We conclude that CIB2 and CIB3 are MET channel auxiliary subunits with striking similarity to $K_V4$ channel auxiliary subunits.

## ETOC Paragraph

Liang et al. demonstrate that CIB2 regulates the function of hair cell mechanotransduction by controlling the distribution of TMC1/2 in hair cells, and by regulating the function of the mechanotransduction channel. Structural studies demonstrate that CIB2 and CIB3 resemble KChIP proteins, regulators of voltage-gated $K_V4$ channels.

## Graphical Abstract

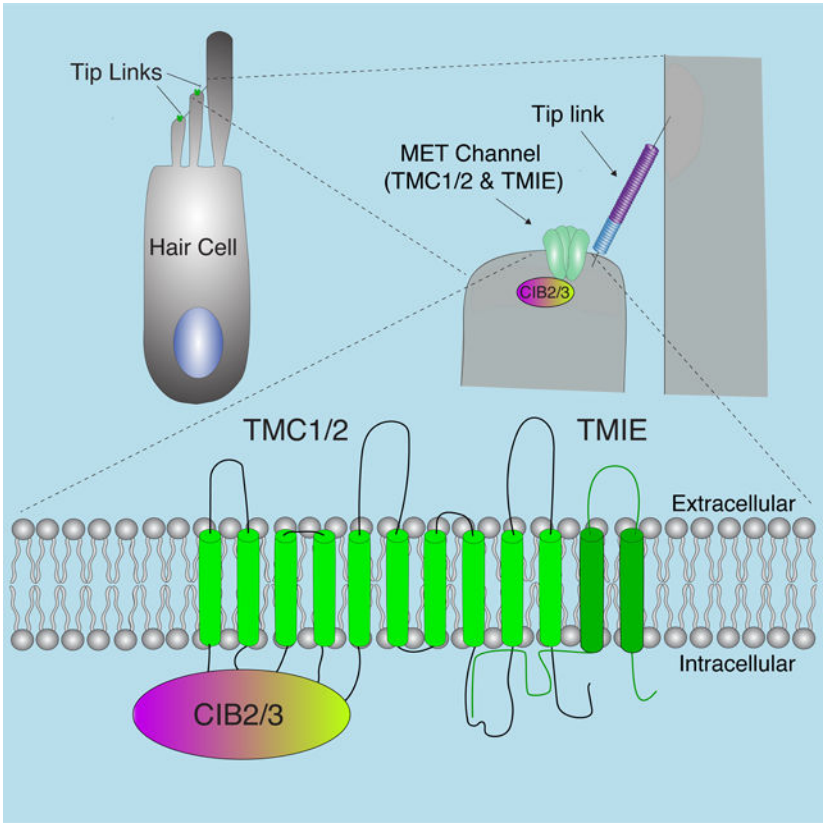


## Introduction

Mechanoelectrical transduction (MET), the conversion of mechanical stimuli into electrochemical signals, is of fundamental importance for organisms to sense a range of external and internal stimuli. In the inner ear, MET channels are localized in the stereocilia of hair cells near tip links, the filaments consisting of CDH23 and PCDH15 that transmit force onto MET channels when stereocilia are deflected (Cunningham and Muller, 2018; Fettiplace, 2017; Maoileidigh and Ricci, 2019). Studies of genes linked to deafness have identified components of the MET channel complex. These include the integral membrane proteins TMC1/2, TMIE, and LHFPL5 (Beurg et al., 2015b; Cunningham et al., 2020; Pan et al., 2018; Pan et al., 2013; Xiong et al., 2012; Zhao et al., 2014) (Fig. 1A). In mice, TMC1

and TMC2 are expressed in vestibular hair cells throughout life, while TMC2 is present in cochlear hair cells only in the first few days after birth before it is progressively replaced by TMC1 (Kawashima et al., 2011; Kim and Fettiplace, 2013; Kurima et al., 2015). No developmentally regulated expression patterns have been reported for TMIE and LHFPL5.

Recent studies suggest that the MET channel in hair cells is a heteromeric complex consisting of TMC1/2 and TMIE. Structural modelling studies, the analysis of mice with mutations in *Tmc1* and *Tmc2*, and in vitro reconstitution experiments provide evidence that TMC1 and TMC2 are pore-forming subunits of the MET channel (Ballesteros et al., 2018; Corns et al., 2016; Goldring et al., 2019; Jia et al., 2020; Kim and Fettiplace, 2013; Pan et al., 2018; Pan et al., 2013). Mutations in TMIE affect the pore and gating properties of the MET channel as well (Cunningham et al., 2020), demonstrating that TMIE is also an integral MET channel subunit. The function of LHFPL5 within the MET channel complex is unclear.

The function of ion channels is frequently regulated by auxiliary subunits. Putative auxiliary subunits of the MET channel in hair cells are the $Ca^{2+}$ and integrin binding protein 2 (CIB2) and its homologue CIB3. Mutations in the gene encoding CIB2 cause hearing loss but no vestibular dysfunction in humans and mice (Patel et al., 2015; Riazuddin et al., 2012; Seco et al., 2016). CIB2 is localized to stereocilia of murine cochlear hair cells, binds to TMC1 and TMC2 and is essential for MET by cochlear hair cells (Giese et al., 2017; Michel et al., 2017; Riazuddin et al., 2012; Wang et al., 2017). For unknown reasons, vestibular hair cells express both CIB2 and CIB3. Vestibular hair cells are also not affected by *Cib2* mutations (Giese et al., 2017), suggesting that in vestibular hair cells CIB3 can compensate for the loss of CIB2. Intriguingly, CIB2 and CIB3 share sequence homology with KChIP proteins, members of the family of neuronal $Ca^{2+}$ sensor (NCS) proteins (Burgoyne et al., 2019). KChIP proteins bind to the N-terminal cytoplasmic tail of $K_v4$ and regulate channel assembly, cell surface expression, and function (An et al., 2000; Wang, 2008). This raises the possibility that CIB2 and CIB3 might similarly be auxiliary subunits of the MET channel. Notably, studies in nematodes suggest that CIB2 might link the MET channel to the cytoskeleton (Tang et al., 2020). However, the atomic structures of CIB2 and CIB3 are not known, and the function of these proteins in mammalian hair cells remains to be elucidated.

Using X-ray crystallography, we show here that CIB2 and CIB3 are structurally similar to KChIP1 and other NCS proteins. A hydrophobic groove in CIB2/3 mediates interactions of CIB2/3 with TMC1, mirroring the interaction of KChIP proteins with $K_v4$ channels. Studies in cochlear hair cells show that CIB2 and CIB3 are functionally interchangeable, and that CIB2 regulates both the assembly and function of the MET channel complex. Overall, our data show that CIB2 and CIB3 are auxiliary MET channel subunits, and that $K_v4$ channel function and MET channel function are regulated by auxiliary ion channel subunits with strikingly similar properties.

## Results

### CIB2 and CIB3 are functionally interchangeable in cochlear outer hair cells

CIB2 is a member of a gene family comprised of four proteins (CIB1–4). Each of these proteins contains four EF-hand motifs, and they share sequence homology (Fig. 1B) and protein domain organization (Fig. 1C) with KChIP1. Among the CIB proteins, CIB2 and CIB3 are the closest relatives (Fig. 1B, Fig. S1A,B) (Gentry et al., 2005). CIB2 is expressed in cochlear hair cells while CIB2 and CIB3 are co-expressed in vestibular hair cells (Giese et al., 2017). The fact that mutations in the gene encoding CIB2 lead to hearing impairment without vestibular involvement (Giese et al., 2017; Michel et al., 2017; Wang et al., 2017) suggests that CIB2 and CIB3 have redundant functions. We therefore determined whether CIB3 could replace CIB2 in cochlear hair cells. For these experiments, we used the *Cib2*$^{tm1a}$ mouse strain from EUCOMM (referred to as *Cib2*$^{-/-}$), which we confirmed were deaf but had no obvious vestibular defects (Fig. S1C-E, not shown). We also recorded MET currents from outer hair cells (OHCs) of *Cib2*$^{-/-}$ mice at postnatal day (P) 6–7 by deflections of hair bundles with a stiff glass probe. MET currents were recorded by patching onto the cell body of hair cells. As reported (Giese et al., 2017; Michel et al., 2017; Wang et al., 2017), MET currents were abolished in *Cib2*-deficient OHCs (Fig. S1F,G).

Next, we expressed by injectoporation (Xiong et al., 2012; Xiong et al., 2014) CIB1, CIB2, and CIB3 in OHCs from *Cib2*$^{-/-}$ mice at P3 and recorded MET currents two days later. Results were compared to recordings from wild-type hair cells (P3 + 2 days in vitro). Because of variability in bundle shape following injectoporation, a probe with approximate bundle size was lowered onto the hair bundle from the top. Both CIB2 and CIB3, but not CIB1, rescued MET defects in OHCs from *Cib2*$^{-/-}$ mice (Fig. 1D-G). Failure of CIB1 to rescue MET was not caused by defects in protein trafficking since immunostaining confirmed that CIB1, CIB2 and CIB3 were localized to stereocilia of injectoporated cells (Fig. 1H). Injectoporated CIB2 led to slightly lower peak amplitudes of MET currents at saturating mechanical stimuli compared to wild-type, but CIB2 was slightly more effective in rescuing transduction compared to CIB3 (680.6 ± 27.2 pA for wild-type; 590.1 ± 28.7 pA for CIB2; 464.1 ± 32.4 pA for CIB3). Plots of the open probability ($P_o$) of the transduction channel against displacement and fitted with a double Boltzmann equation (Fig. 1F, Fig. S1H,I) revealed that one of the slopes (Z2) was slightly decreased in hair cells expressing CIB3 compared to hair cells from wild-type or those injectoporated to express CIB2 (13.90 ± 0.91 $\mu m^{-1}$ for wild-type; 13.76 ± 0.81 $\mu m^{-1}$ for CIB2; 10.00 ± 0.84 $\mu m^{-1}$ for CIB3). Resting $P_o$ was also increased (2.09 ± 0.17 % for wild-type; 2.79 ± 0.30% for CIB2; 4.64 ± 0.62% for CIB3) in hair cells expressing CIB3 (Fig. 1I, Fig. S1H,I).

We next analyzed ion selectivity of the MET channel in CIB2- and CIB3-expressing OHCs by determining the reversal potential. We measured the peak amplitude of MET currents in various holding potentials from −144 mV to +136 mV stepwise with 20mV intervals (Fig. 1J). We calculated the reversal potential from current/voltage curves (Fig 1K). Fig. 1L shows normalized curves. We did not observe a significant difference in reversal potential between OHCs expressing CIB2 or CIB3 (3.49 ± 1.09 mV for CIB2; 3.49 ± 1.08 mV for CIB3, Fig. 1M).

We conclude that CIB2 and CIB3 are largely functionally interchangeable in OHCs. Small differences in peak amplitude, resting $P_o$, and Z2 in hair cells expressing CIB2 versus CIB3 could be a consequence of differences in protein expression levels, hair bundle shape of cultured hair cells, or protein function.

## CIB2 regulates the distribution of TMC1 in cochlear hair cells

Although previous studies suggested that CIB2 is not essential for TMC1 localization to stereocilia (Giese et al., 2017), we re-investigated this point by taking advantage of *Tmc1*$^{HA}$ and *Tmc2*$^{MYC}$ mouse lines, in which we introduced sequences encoding HA- and MYC-tags in frame at the C-termini of the endogenous *Tmc1* and *Tmc2* genes, respectively (Fig. 2A) (Cunningham et al., 2020). The epitopes do not affect TMC1/2 function (Cunningham et al., 2020). Consistent with RNA expression and functional data from wild-type mice (Kawashima et al., 2011; Kim and Fettiplace, 2013; Kurima et al., 2015), TMC2-MYC expression increases in cochlear hair cells between P0 and P3 and is downregulated by P5–7. TMC1-HA expression is low until P3 but thereafter is upregulated (Cunningham et al., 2020).

We generated mice homozygous for the *Cib2*$^{-/-}$ mutation and for epitope-tagged TMC proteins, and analyzed TMC2-MYC and TMC1-HA localization by immunohistochemistry in cochlear whole mounts between P4 and P8 (Fig. 2B,C). For a quantitative assessment of fluorescence signals, we used Imaris 9.1 to analyze the expression using optical sections through the entire hair bundle (Fig. 2D,E). Localization of TMC1 and TMC2 to stereocilia was detected in heterozygous *Cib2*$^{+/-}$ control mice but was undetectable in *Cib2*$^{-/-}$ mice (Fig. 2B,C). TMC1 was still expressed in the cell body of *Cib2*$^{-/-}$ mutant mice (Fig. 2B). These findings are consistent with the finding that MET is completely abolished in *Cib2*$^{-/-}$ mice and indicate an important function for CIB2 in the trafficking or retention of TMC1/2 in stereocilia.

When TMC1 is expressed in heterologous cells, it remains in the ER (Cunningham et al., 2017; Giese et al., 2017; Labay et al., 2010; Zhao et al., 2014). We wondered whether TMC1 localization might change upon co-expression with CIB2. We transfected HAP-1, HEK293 and COS-7 cells to co-express CIB2 and TMC1-GFP (Fig. 2F-H). To label the plasma membrane, we co-expressed TMIE-HA. F-actin was visualized by phalloidin staining. Protein distribution was analyzed by immunocytochemistry (Fig. 2G,H). Expression of CIB2 (and TMIE) did not affect the distribution of TMC1-GFP, which was retained inside cells. We thus conclude that CIB2 (and TMIE) are not sufficient to achieve cell surface expression of TMC1 in heterologous cells.

## TMC1 binds CIB2 and CIB3

Previous studies have shown that a protein fragment encompassing amino acid 81–130 in the N-terminal domain of mammalian TMC1 bind to CIB2 (Giese et al., 2017; Tang et al., 2020). We wanted to further define interactions between TMC1 and CIB2 using full-length proteins with the goal to identify mutations that disrupt complex formation and to functionally evaluate them. We co-expressed TMC1 with CIB1, CIB2, CIB3, and KChIP1 in HEK cells for co-immunoprecipitation experiments. To facilitate the

experiments, we introduced a MYC-tag at the N-terminus of TMC1 and a HA-tag at the N-termini of CIB1, CIB2, CIB3, and KChIP1 (Fig. 3A). Cell extracts were prepared ~36 hours after transfection. Protein complexes were isolated by immunoprecipitation with anti-MYC antibodies and resolved on SDS-PAGE gels. Co-immunoprecipitating proteins were detected by western-blotting using anti-HA antibodies. As controls, we analyzed the input amount of the epitope-tagged proteins prior to immunoprecipitation and total amount of MYC-TMC1 captured with the MYC antibody (Fig. 3B). Quantification of the results (≥ 3 experiments) demonstrated that HA-CIB2 and HA-CIB3, but not HA-CIB1 or HA-KChIP1, efficiently co-immunoprecipitated with MYC-TMC1 (Fig. 3B). TMC1 proteins were resolved on gels into several bands. Based on molecular weight, the fastest migrating band corresponded to monomeric TMC1 while other bands likely represented multimers and/or post-translationally modified proteins.

CIB2 preferentially binds $Mg^{2+}$ over $Ca^{2+}$ (Vallone et al., 2018). Under physiological conditions CIB2 is likely bound by $Mg^{2+}$ because of the relative high concentration of $Mg^{2+}$ in cells (0.5–1.0 mM) (Romani and Scarpa, 2000). In contrast, $Ca^{2+}$ fluctuates in the range of 0.1–20 μM (Berridge et al., 2003), although local concentration may differ during cell signaling. To analyze whether divalent ions affect CIB2 interactions with TMC1, we co-expressed the two proteins in HEK-293 cells and carried out co-immunoprecipitation experiments under varying conditions: (i) in the absence of $Ca^{2+}$ and $Mg^{2+}$; (ii) in the presence of 5 mM $Ca^{2+}$ only, or $Mg^{2+}$ only; (iii) in the presence of 5 mM EDTA or EGTA. There was no detectable difference in the interaction between TMC1 and CIB2 in any of these conditions (Fig. S2A).

## Identification of a new CIB2 binding domain in TMC1

To map domains in TMC1 that mediate CIB2 binding, we generated MYC-TMC1 deletion constructs for co-immunoprecipitation experiments with HA-CIB2 (Fig. S2B). Unlike in previous studies that carried out experiments with an N-terminal fragment of TMC1 (Giese et al., 2017), we analyzed truncations of the full-length TMC1 protein. Truncations were named according to the amino acids after which the protein was truncated. MYC-TMC1/1-396 bound as efficiently to HA-CIB2 as full length TMC1 (Fig. S2C). Additional truncations indicated a weak binding site in the predicted N-terminal cytoplasmic domain (TMC1/1-170) consistent with earlier data (Giese et al., 2017), and a newly identified major binding site within the first cytoplasmic loop domain between transmembrane domain 2 and 3 (TMC1/298-352) (Fig. S2B,D).

We next introduced deletions of 3-We next introduced deletions of 3–13 amino acids into full-length MYC-TMC1 (Fig. S3A). These experiments confirmed two domains in MYC-TMC1 contributing to CIB2 binding. The first domain encompasses amino acids 100–121 (Fig. S3B). The second domain encompasses amino acids 305–344 (Fig. S3B).

Since deletions might disrupt protein structure, we introduced double and triple point mutations into TMC1 (Fig. 3C,D). Consistent with the deletion mutations, triple point mutations converting amino acids 305–307, 309–311, 315–318, or 336–338 to Ala drastically reduced binding of CIB2 to TMC1, while different mutations between amino acid 100–121 had less or no effect (Fig. 3C,D).

Interactions of KChIP1 with $K_V4$ is mediated by a hydrophobic groove in KChIP1 (Pioletti et al., 2006; Scannevin et al., 2004; Wang et al., 2007; Zhou et al., 2004). Interaction of MYC-TMC1 with HA-CIB2 was observed in 1.2 M NaCl (Fig. S3C), suggesting that interactions between MYC-TMC1 and HA-CIB2 may also rely on hydrophobic interactions.

## Crystal structures of the CIB3 dimer

We attempted to determine the structure of CIB2 and CIB3 by X-ray crystallography but were unable to obtain diffraction-quality crystals of CIB2, and thus focused on CIB3. Consistent with the observation for CIB2 (Vallone et al., 2018), CIB3 showed evidence of dimerization. Monomer and dimer peaks were observed in size-exclusion chromatography (SEC) for CIB3 (Fig. S5A) as confirmed by the corresponding masses characterized by in-line multi-angle light scattering (MALS) measurements (not shown). We determined the structure for CIB3 in two crystal forms to 1.88 Å and 1.83 Å (Fig. 4A,B). The structure for crystal form 1 (Fig. 4A; Table S1), was determined by molecular replacement using the crystal structure of CIB1 (PDB: 1XO5) as a search model. The structure for crystal form 2 (Fig. 4B; Table S1) was of a double mutant CIB3 EK150151QH, designed to aid in crystallization, and was determined using the crystal form structure 1 as a search model.

The two crystal structures (Fig. 4A,B) showed CIB3 to form a domain-swapped dimer, with the twelve most C-terminal residues bound in a hydrophobic trench in the partner molecule. Although CIB1 is monomeric (Gentry et al., 2005), the topology of the CIB3 protomer is highly similar to CIB1, with nine α-helices, eight of which participate in four EF-hand motifs. EF hand-canonical $Ca^{2+}$-binding residues are conserved in the two C-terminal EF hands of CIB3 (EF-hand 3, helices 6–7; EF-hand 4 helices 8–9), but are incomplete or absent in the two N-terminal EF hands (EF-hand 1, helices 2–3; EF-hand 2 helices 4–5). EF-hand 1 does not contain any canonical $Ca^{2+}$-binding residues and contains an inserted extended loop. EF-hand 2 contains a Ser in place of a canonical $Ca^{2+}$-binding motif Asp/Glu at position 71.

The CIB3 protomer structures are similar in each crystal form, with root-mean-square deviations (RMSDs) between 168 corresponding Cα atoms of 0.573 Å for protomers of crystal form 1 and 0.843 Å for protomers of crystal form 2. CIB3 protomers are also similar between the two crystal forms, with the RMSDs of aligned Cα atoms for one protomer in crystal form 1 to promoters of crystal form 2 of 0.866 Å and 0.837 Å; the other protomer of crystal form 1 showed RMSDs of 0.931 Å and 0.692 Å to the protomers of crystal form 2. For all alignments and RMSD calculations, residues 5–174 were used, to exclude the highly variable C-terminus.

Larger differences between the two crystal forms (Fig. S4A) were observed for dimeric CIB3, consistent with the structural variability of C-terminal residues. In crystal form 1, the protomers are related by a non-crystallographic two-fold axis, with the centers of mass between promoters spaced 36.6 Å apart. In crystal form 2, the protomers are related by a 166° rotation around a non-crystallographic axis, with the centers of mass only 29.6 Å apart. When one chain of the first crystal is superposed on one chain of the second crystal, the Euler angle between the two unaligned protomers is 80.42°, with a 25 Å shift in the centers of mass (Fig. S4A).

Each protomer of crystal form 1 showed only a single $Ca^{2+}$ ion bound at EF-hand 3, while in crystal form 2 EF-hands 3 and 4 had bound $Ca^{2+}$ ions. To confirm the identity of bound ions, we utilized the anomalous diffraction from data measured at 8.5 keV x-ray energy to generate Bijvoet difference maps to visualize $Ca^{2+}$ (Figure S4B,C). EF-hands 1 and 2, which lack canonical $Ca^{2+}$ ligands, showed no evidence of $Ca^{2+}$ binding, but the Bijvoet difference maps showed anomalous density for EF-hand 3 in both crystal forms (Fig. S4B,C; upper panels). Crystal form 2 also showed anomalous density for a $Ca^{2+}$ ion bound in EF-hand 4. This difference in occupancy of EF-hands likely resulted from differences in $Ca^{2+}$ concentrations during crystallization (crystal form 1 and 2 were grown in the presence of 5 mM $Ca^{2+}$ and 200 mM $Ca^{2+}$, respectively).

The CIB3 dimer is formed through the domain-swapped binding of the C-terminal segment between the two protomers with an interface surface area of 2017.3 $Å^2$ for crystal form 1, and 1764.1 $Å^2$ for crystal form 2. The swapped C-termini are anchored by a pair of aromatic residues, Phe179 and Phe183, from the C-terminus of each protomer binding in a large hydrophobic trench in the other (Fig. S4D). These Phe residues are nearly completely buried in the dimer interface (>90%) and contribute ~15% of the total interface surface area. The hydrophobic trench of CIB3 that binds the C-terminus is lined by residues Phe70, Ile74, Phe78 on helix four; Met98 on helix five; Tyr110, Ala111, Ile114, Tyr115 on helix six; Leu128, Thr131, Val132, Leu135 on helix seven; Val152 on helix eight; and Phe169, Met172 on helix nine.

## Crystal structure of CIB3 in complex with the newly identified interacting domain of TMC1

To understand the interaction between CIB2/3 and TMC1, we attempted to co-express CIB3 with TMC1 fragments (amino acid 298–344, 298–352, 298–355, 298–359). The only TMC1 fragment that crystallized with CIB3 contained amino acids 298–352, which includes the major binding site for CIB3 within the first intracellular loop domain of TMC1. Size-exclusion chromatography (SEC) revealed this fragment to form a complex with CIB3, which behaved as a monomer when bound to the TMC1 fragment (Fig. S5B). We purified this complex by SEC, and determined its structure to 1.83 Å resolution (Fig. 4C) by molecular replacement using one CIB3 protomer from the crystal form 1 CIB3 dimer structure as a search model (Table S1).

The refined map for the TMC1:CIB3 complex structure revealed electron density for forty-five residues (303–347) of the TMC1 peptide, which was folded into two α-helices, with the N-terminal helix eight residues in length and the C-terminal helix twenty-six residues. These helices are connected by an eight-residue linker comprised of residues 314–321. The TMC1 peptide binds to CIB3 primarily through elements of the N-terminal α-helix and the linker, occupying the same hydrophobic trench that accommodates the C-terminus in the domain-swapped dimer. The interface between the TMC1-peptide and CIB3 buries 1583.8 $Å^2$ surface area between the two molecules. The CIB3:TMC1-peptide interaction is anchored by two aromatic residues in TMC1, Phe312 and Tyr317, similar to Phe179 and Phe183 in the CIB3 C-terminus-swapped dimer. Phe312 and Tyr317 constitute ~21% of the interfacial surface area (Fig. 4C,D), with significant contributions from a few other residues including Val311 and Trp315. The long C-terminal helix of the TMC1 peptide,

corresponding to residues 322–347, contacts CIB3 α-helices 7 and 8, and is stabilized by hydrophobic interactions between TMC1 residues Leu332 and Phe336 with CIB3 residues Val132, Leu135, and Val148. In addition, two salt bridges are formed between the TMC1 Asp326 and CIB3 Arg137 and TMC1 Arg344 and CIB3 Glu143.

CIB3 binding by TMC1 displaces the CIB3 C-terminus that underlies dimer formation. As the binding site for TMC1 on CIB3 overlaps the dimer-binding site for the C-terminus, many of the interfacial residues are the same. Of the fifteen hydrophobic-trench residues participating in C-terminus binding listed above, twelve take part in the TMC1 interface. The three residues that differ, Phe78, Tyr110, and Ala111, are occluded from interacting with TMC1 by the C-terminus of CIB3. In the TMC1:CIB3 complex structure, the CIB3 C-terminus sits to one side of the trench, contributing to the binding interface (Fig. 4C,D). Additionally, four residues, 179–182, fold into a small α-helix connected to the end of the α9-helix by a three-residue linker. The last five residues of the carboxy terminus are extended and positioned at the edge of the binding trench, with the terminal carboxylic acid group forming a salt bridge with Arg29.

The crystallization condition for the CIB3:TMC1 complex contained 5 mM $CaCl_2$ and 200 mM $MgCl_2$, and CIB3 EF-Hands 3 and 4 are occupied by $Mg^{2+}$ rather than $Ca^{2+}$. As expected for $Mg^{2+}$, the ions show octahedral coordination in both EF hands, and while Bijvoet difference maps (measured at 7 keV x-ray energy) show an absence of anomalous density in the metal-ion binding position (as expected for $Mg^{2+}$), the peak for the sulfur atom of cysteine 124 is clearly visible (Fig. 4D, right panels). Despite the coordination of $Mg^{2+}$, no significant changes in Cα positions were observed for the EF-hand residues. RMS coordinate differences for each EF-hand between the $Mg^{2+}$-bound CIB3:TMC1 complex and the $Ca^{2+}$-bound crystal form 1 CIB3 dimer structure are 0.460 Å for EF-hand 3 and 0.568 Å for EF-hand 4. Since the complex was co-purified in the presence of $Ca^{2+}$, this suggests that $Mg^{2+}$ binding may be a result of the high $Mg^{2+}$ concentration of the crystallization condition and not a requisite for complex formation.

The binding pocket for TMC1 on CIB3 is highly conserved. We used the program ConSurf (Landau et al., 2005) to map conservation between CIB3 proteins from different species to the surface of CIB3 (Fig. 4E). The most conserved residues of CIB3 are those in close proximity to the domain-swap dimerization/TMC1-binding site. The residues on TMC1 involved in CIB3 binding are conserved in TMC1 and TMC2, but less in other TMCs, as revealed by a sequence logo for the CIB3-binding domain of TMC1 and TMC2, corresponding to the first α-helix and linker domain (Fig. 4F,H) (Crooks et al., 2004). Phe312 and Tyr317 are conserved, with Trp315 and Asp316 showing near total conservation. While Trp315 makes hydrophobic contacts with CIB3, the side chain of Asp316 is directed away from CIB3, and its function is not apparent from the TMC1:CIB3 complex structure.

Homology modeling reveals strong correlation in the pattern of conservation in the structure of CIB2 and CIB3, with residues of highest conservation clustered around the hydrophobic groove that mediates TMC1/2 binding (Fig. 4E,G; Fig. S5G). By contrast, CIB1 has numerous differences in amino acid identity for residues within the hydrophobic groove

and a four-residue insert in the loop between EF-hands 3 and 4 that would sterically clash with the larger helix in TMC1 (Fig. S5H).

While the binding pocket on CIB3 is analogous to the one observed for $K_V4$ on KChIP1, there is a difference in the orientation of the TMC1 peptide. In CIB3:TMC1, the TMC1 peptide is approximately parallel to the C-terminus of CIB3 (Fig. S5E), whereas in KChIP1:$K_V4$, the $K_V4$ peptide is approximately antiparallel to the C-terminus of KChIP1 (Fig. S5F).

## Mutational analysis of the contact surface of TMC1 with CIB2 and CIB3

Our data suggest that CIB2 and CIB3 are highly similar in structure (Fig. 4E,G; Fig. S5E-G) and bind to TMC1 through a conserved binding pocket. To corroborate the structural data and to further confirm that CIB2 and CIB3 bind to TMC1 by a similar mechanism, we generated TMC1 constructs containing point mutations at Phe312, Trp315, Tyr317, Ile332 and Phe336, which are predicted to be important for binding to CIB2 and CIB3, and Asn321, Glu323 and Lys337, which are not (Fig. 5A). Phe312Arg, Trp315Asp, Ile332Asp, and Phe336Asp were designed to disrupt hydrophobic interactions by introducing a buried charge Asp or a bulky charged Arg. Tyr317Ala removed hydrophobic interfacial surface area. We tested a few mutants that should have no effect. Asn321Lys and Glu323Lys introduce a larger charged residue, but since they remain in solvent they should have no effect on TMC1:CIB2 or TMC1:CIB3 binding. Lys337Gln disrupts an interaction between solvent-exposed Lys323 and the main chain carboxyl group of CIB3, while Glu139 should not affect binding (Fig. 5A, Fig. S6A,B).

We co-expressed eight mutant MYC-TMC1 constructs with wild-type HA-CIB2 (Fig. 5A,C) or HA-CIB3 (Fig. S6A,B) in HEK cells and carried out co-immunoprecipitation experiments with HA antibodies. MYC-TMC1 was detected by western-blotting using antibodies to MYC. As predicted from the structural data, the Phe312Arg, Trp315Asp, Tyr317Ala, Ile332Asp and Phe336Asp mutations in TMC1 disrupted interactions of MYC-TMC1 with HA-CIB2 and HA-CIB3, while the Asn321Lys, Glu323Lys and Lys337Gln mutations had no effect on binding (Fig. 5C, Fig. S6C).

We also introduced point mutations into CIB2 and CIB3 predicted to affect interactions with TMC1 to varying degrees. Asn68Gln extends Asn68 by an extra carbon atom, which would occlude binding of TMC1 residues Trp315 and Tyr317. Ile114Phe swaps Ile for a bulkier Phe. Thr131Leu makes CIB2 and CIB3 more similar to CIB1. Leu140Arg buries a bulky charged residue into the interface. Both Val148Phe and Val152Phe change the smaller Val to a larger Phe (Fig 5B, Fig. S6D,E). As predicted, the Asn68Gln, Ile114Phe, Leu140Arg and Val152Phe mutations in CIB2 and CIB3 affected interactions of HA-CIB2 and HA-CIB3 with MYC-TMC1, while the remaining mutations had little effect (Fig. 5D, Fig. S6F; note that Val148Phe mildly affected interactions with CIB2).

Amino acids that affect binding are conserved between TMC1 and TMC2 (Fig. 5A, Fig. S6A) and between CIB2 and CIB3 (Fig. 5B, Fig. S6D) but they are not all conserved in other TMC proteins (Fig. 4G, data not shown) or in CIB1 and CIB4 (Fig. 5B, Fig.

S6D). Given the high degree of structural conservation between CIB2 and CIB3, subsequent functional studies were carried out with CIB2.

## Mutations in CIB2 that disrupt TMC1 binding affect MET

To determine whether interactions of CIB2 with TMC1 are critical for MET, we expressed by injectoporation CIB2 point mutations in OHCs from *Cib2*$^{-/-}$ mice at P3 and recorded MET currents two days later. Wild-type CIB2 and the point mutant constructs changing Ile114 to Phe (CIB2-I114F) and Tyr131 to Leu (CIB2-T131L), showed significant binding to TMC1 and rescued MET defects in OHCs from *Cib2*$^{-/-}$ mutant mice (Fig. 5E). Point mutant constructs changing Asn68 to Gln (CIB2-N68Q) and Val152 to Phe (CIB2-V152F), which disrupt interactions with TMC1, did not rescue MET (Fig. 5E). Current displacement (I/X) plots were fitted with a double Boltzmann equation and revealed that peak currents were not significantly different between wild-type CIB2, CIB2-I114F and CIB2-T131L (656.8 ± 31.5pA for CIB2; 611.6 ± 26.9 pA for CIB2-I114F; 517.1 ± 58.6 pA for CIB2-T131L, Fig. 5F,G). When we plotted the open probability of the transducer channel ($P_o$) against displacement, the resulting curves for mutants were slightly but not significantly shifted to the right (Fig. 5F), indicating that the sensitivity of transducer currents to hair bundle deflection was similar in OHCs expressing wild-type CIB2 and the CIB2-I114F as well as the CIB2-T131L mutation (Fig. 5F). Slopes of curves were less steep than in recordings of acutely isolated hair cells because hair bundle shape was somewhat altered due to injectoporation. Notably, wild-type CIB2 and the point mutant CIB2 proteins localized to stereocilia of OHCs (Fig. 5H), indicating that failure to rescue MET by CIB2-N68Q and CIB2-V152F was not a consequence of defects in their ability to localize to stereocilia.

We conclude that complex formation between CIB2 and TMC1 (and likely TMC2) is critical for CIB2 function in hair cells.

## CIB2 point mutations linked to deafness affect TMC1 and TMC2 binding

We next wanted to ask whether *Cib2* point mutations linked to deafness affect mechanotransduction by disrupting CIB2 binding to TMC1/2. Six point mutations have been described in CIB2 that cause deafness (Fig. 6A,B) (Patel et al., 2015; Riazuddin et al., 2012; Seco et al., 2016). The amino acids affected by the point mutations are conserved between mouse and human, and map to the domain of CIB2 with highest conservation to CIB3. Using co-immunoprecipitation experiments, we observed that the six mutations reduced but did not abolish binding of CIB2 to TMC1 and TMC2 (Fig. 6C, Fig. S7A,B). The CIB2-F91S and CIB2-I123T mutations reduced TMC1/2 binding most severely, while other mutations had less of an effect (Fig. 6C). All six mutant CIB2 proteins localized to stereocilia of OHCs from *Cib2*$^{-/-}$ mutant mice injectoporated to express the constructs (Fig. 6D).

To further define the mechanism by which *Cib2* point mutations linked to deafness affect hair cell function, we engineered mouse lines carrying point mutations in the endogenous *Cib2* mouse gene (Fig. 6E). We focused on three mouse lines carrying the following mutations: (i) CIB2-I123T, severely affecting binding of CIB2 to TMC1 and TMC2; (ii) CIB2-E64D and (iii) CIB2-R186W, both of which perturb binding to TMC1 and TMC2 less severely (Fig. 6C, Fig S7B). Mice homozygous for the *Cib2* point mutations

were deaf as determined by measurement of the auditory brain stem response (ABR) for click stimuli (Fig. 6F) and pure tones (Fig. 6G). Next, we recorded MET currents from OHCs of the mutant mice (Fig. 7A-D). At P5-P6, MET currents were abolished in OHC from *Cib2*$^{I123T/I123T}$ mice (Fig. 7B), and were severely reduced, in *Cib2*$^{E64D/E64D}$ and *Cib2*$^{R186W/R186W}$ mice (Fig. 7C,D). We also plotted the data for *Cib2*$^{E64D/E64D}$ and *Cib2*$^{R186W/R186W}$ as open probability versus deflection to normalize for differences in peak currents compared to wild-type. We observed that the resting open probability $P_o$ appeared slightly elevated in OHCs from *Cib2*$^{E64D/E64D}$ (2.68 ± 0.07 % in control; 6.82 ± 0.36 % in *Cib2*$^{E64D/E64D}$; **, P<0.01) and *Cib2*$^{R186W/R186W}$ (2.05 ± 0.17 % in control; 4.18 ± 0.24 % in *Cib2*$^{R186W/R186W}$; *, P<0.05) mice (Fig. 7C,D). We conclude that mechanotransduction is less severely affected by point mutations that have the mildest effects on binding of CIB2 to TMC1 and TMC2 (R186W, E64D) compared to a point mutation that nearly completely abolishes binding (I123T).

## CIB2 mutations linked to deafness differentially affect TMC1 and TMC2 localization to hair bundles

Defects in mechanotransduction caused by CIB2 mutations linked to deafness could be a consequence of defects of TMC1 and TMC2 transport into stereocilia due to weakened interactions between the proteins. To test this hypothesis, we generated mice homozygous for *Cib2* mutations and for epitope-tagged TMC proteins and analyzed TMC2-MYC and TMC1-HA localization by immunohistochemistry in cochlear whole mounts between P4 and P8 (Fig. 7E-I). For a quantitative assessment of fluorescence signals, we used Imaris 9.1 to analyze the expression using optical sections through the entire hair bundle. Localization of TMC1 and TMC2 to stereocilia was detected in heterozygous *Cib2*$^{+/-}$ control mice but was undetectable in *Cib2*$^{-/-}$ and *Cib2*$^{I23T/I123T}$ mice (Fig. 7E,H,I), consistent with lack of MET in OHCs from these mice. In contrast, the immunofluorescence signal for TMC1-HA in stereocilia from *Cib2*$^{E64D/E64D}$ mutant mice was reduced but not abolished at P6 compared to controls; this defect was more pronounced by P8 (Fig. 7F,H). The immunofluorescence signal for TMC2-MYC was also reduced in the *Cib2*$^{E64D/E64D}$ mutants at P4, when TMC2 levels are highest in control mice (Fig. 7G,I) (Cunningham et al., 2020). TMC1-HA immunofluorescence signals were undetectable in stereocilia of *Cib2*$^{R186W/R186W}$ mice at all ages analyzed (Fig. 7F,H), while TMC2-MYC was still detectable at P4, albeit at reduced level compared to wild-type (Fig. 7G,I). Notably, TMC1 levels in the cell bodies of the mutants was unaltered (Fig. S7C), further indicating that protein localization and not expression was affected by the mutations.

Our data suggested that TMC2 is responsible for the remaining transducer currents in *Cib2*$^{R186W/R186W}$ mice. To confirm these findings, we crossed *Cib2*$^{R186W/R186W}$ mice with *Tmc2*-deficient mice (*Tmc2*$^{-/-}$) to obtain *Cib2*$^{R186W/R186W}$;*Tmc2*$^{-/-}$ mice. As predicted, no transducer currents could be recorded from the offspring (Fig. S7D,E).

We conclude that defects in MET in mice with *Cib2* mutations can be explained at least in part by defects in the localization of TMC1 and TMC2 to stereocilia. Some point mutations are hypomorphic since they affect TMC1 and TMC2 localization only partially.

## Effects of CIB2 point mutations on resting $P_o$

We next wanted to analyze the function of transduction channels in mice with mutations in CIB2 more closely. The properties of transduction channels containing TMC1 and TMC2 differ (Beurg et al., 2014; Goldring et al., 2019; Kim et al., 2013; Kim and Fettiplace, 2013). Since both TMC1 and TMC2 are expressed in wild-type hair cells, and since CIB2 mutations differentially affect TMC1 and TMC2 transport into stereocilia, we wanted to ensure that we analyzed effects of Cib2 mutations on one TMC protein only. We focused our analysis on *Cib2*$^{R186/R186W}$ mice, which had the largest remaining transducer currents of all mutants analyzed. In these mice, transducer current is dependent on TMC2 only (Fig. S7D,E). As an additional safeguard, we crossed the *Cib2*$^{R186WR186W}$ mutation on a *Tmc1*$^{dn/dn}$ background (Kurima et al., 2002) and compared the phenotype of the resulting *Tmc1*$^{dn/dn}$;*Cib2*$^{R186W/R186W}$ mutants to *Tmc1*$^{dn/dn}$;*Cib2*$^{R186W/+}$ control mice.

Transduction channels are not completely closed at rest and resting $P_o$ depends on the extracellular and intracellular $Ca^{2+}$ concentration (Fettiplace, 2017; Maoileidigh and Ricci, 2019). We analyzed whether CIB2, which can bind $Ca^{2+}$, is critical for the regulation of resting $P_o$. Given the localization of CIB2 intracellularly, we reasoned that changes in the intracellular $Ca^{2+}$ concentration might regulate CIB2 function. We analyzed resting $P_o$ in the presence of 1.3 mM extracellular $Ca^{2+}$, and 1mM or 10mM intracellular BAPTA, to chelate intracellular $Ca^{2+}$. MET currents were evoked in OHCs from *Tmc1*$^{dn/dn}$;*Cib2*$^{R186W/+}$ and *Tmc1*$^{dn/dn}$;*Cib2*$^{R186W/R186W}$ mice with a fluid jet and under holding potentials from −104 mV to +96 mV (Fig. 8A). Resting $P_o$ in OHCs from *Tmc1*$^{dn/dn}$;*Cib2*$^{R186W/+}$ was higher in 10mM BAPTA compared to 1mM BAPTA at all holding potentials analyzed. Resting $P_o$ was also increased in OHCs from *Tmc1*$^{dn/dn}$;*Cib2*$^{R186W/R186W}$ in 10mM BAPTA compared to 1 mM BAPTA (Fig. 8B), but it was substantially higher than in control OHCs at both BAPTA concentrations.

We next analyzed the current-voltage relationship in two different extracellular $Ca^{2+}$ concentrations. Peak currents were recorded in OHCs from P4–5 mice in 1.3 mM and 0.05 mM extracellular $Ca^{2+}$ at various holding potentials ranging from −144mV to +136mV (Fig. S8A). Similar to OHCs from *Tmc1*$^{dn/dn}$;*Cib2*$^{R186W/+}$ mice, MET currents in OHCs from *Tmc1*$^{dn/dn}$;*Cib2*$^{R186W/R186W}$ mutant mice were significantly reduced at negative holding potentials when increasing the extracellular $Ca^{2+}$ concentration from 0.05 mM to 1.3 mM (Fig. S8B).

Taken together, our data suggest that CIB2 regulates resting $P_o$ in TMC2-expressing OHCs by a mechanism that is dependent on the intracellular $Ca^{2+}$ concentration and is affected by the R186W mutation.

## Adaptation is not affected in R186W mutant mice

In hair cells responsive to low frequencies, resting $P_o$ is thought to depend on adaptation. Two distinct adaptation mechanisms have been described, progressing on a fast and a slow time constant, both of which depend on $Ca^{2+}$ entry through MET channels. During fast adaptation, $Ca^{2+}$ has been proposed to act directly on the channel or a molecule near the channel (Cheung and Corey, 2006; Choe et al., 1998; Crawford et al., 1989, 1991; Gillespie

and Muller, 2009). Slow adaptation is thought to depend on the movement of a myosin motor protein that senses tension by the MET channels in a $Ca^{2+}$-dependent manner (Assad and Corey, 1992; Assad et al., 1989; Holt et al., 2002; Howard and Hudspeth, 1987). However, this model appears not to be valid for mammalian cochlear hair cells, where altering $Ca^{2+}$ entry or internal $Ca^{2+}$ buffering have little effect on adaptation, and where resting $P_o$ is not simply a function of adaptation (Peng et al., 2013; Peng et al., 2016) (however see (Beurg et al., 2015a; Corns et al., 2014). We therefore analyzed whether CIB2 affects adaptation.

As we did for the analysis of resting $P_o$, we compared adaptation in OHCs from *Tmc1*$^{dn/dn}$;*Cib2*$^{R186W/+}$ and *Tmc1*$^{dn/dn}$;*Cib2*$^{R186W/R186W}$ mice. Adaptation was evaluated in OHCs from P4–5 mice in two ways. First, MET currents were evoked by 400nm probe deflections for 50 ms, and the decay from the peak of the inward current to the end of the mechanical stimulus was fitted with a double exponential equation (Fig. 8C). The fast and slow time constant and extent of adaptation showed no significant differences between *Tmc1*$^{dn/dn}$;*Cib2*$^{R186W/+}$ and *Tmc1*$^{dn/dn}$;*Cib2*$^{R186W/R186W}$ mice (Fig. 8D). Second, we analyzed adaptation in OHCs using a paired pulse stimulation protocol in which two series of brief mechanical test steps (1 ms) were delivered to the hair bundle with or without a 5 ms non-saturating adaptation step (0.1–0.6 μm) (Fig. 8E-G). Adaptive shifts ($\Delta X_0$/Step), which were calculated from the linear plots of change in the $X_0$ ($\Delta X_0$) with adapting step size (Fig. 8G), were not significantly different between *Tmc1*$^{dn/dn}$;*Cib2*$^{R186W/+}$ and *Tmc1*$^{dn/dn}$;*Cib2*$^{R186W/R186W}$ mice. Previous studies have shown that MET current reduction slows adaptation, probably due to reduced influx of $Ca^{2+}$ into hair cell (Kennedy et al., 2003; Ricci and Fettiplace, 1997). We did not observe this effect, which could perhaps be explained by the fact that we only recorded TMC2-dependent currents. Clearly, extent and time course of adaptation depends on whether TMC1 or TMC2 is expressed (Goldring et al., 2019).

Taken together, our findings are consistent with the model that CIB2 regulates resting $P_o$, but that resting $P_o$ and adaptation at least of TMC2-dependent transducer channels in OHCs are regulated by distinct mechanisms.

## Alterations in the $Ca^{2+}$ permeability and unitary conductance of the MET channel in *Cib2*$^{R186W/R186W}$ mice

We next analyzed effects of the *Cib2*$^{R186W/R186}$ mutations on the $Ca^{2+}$ permeability of the MET channel of OHCs by determining the reversal potential of the channel. Hair cells were recorded with $Ca^{2+}$ and $Cs^{+}$ as the only permeant cations in external and internal solutions, respectively (Kim and Fettiplace, 2013, Pan et al., 2013, Kim et al., 2013, Cunningham et al., 2020). We measured the peak amplitude of MET currents obtained in various holding potentials from −89 mV to +111 mV with 20mV steps (Fig. S8C-H) and calculated the reversal potential from current/voltage curves. Fig. S8D shows absolute values, and Fig. S8F normalized values to account for differences in absolute values between controls and mutants. Fig. S8E shows an enlargement of data in Fig. S8D. The reversal potential (Fig. 8G; 27.81 ± 0.61 mV in *Tmc1*$^{dn/dn}$;*Cib2*$^{R186W/+}$; 23.11 ± 0.67 mV in *Tmc1*$^{dn/dn}$;*Cib2*$^{R186W/R186W}$) and relative $Ca^{2+}$ permeability (Fig. 8H; 5.42 ± 0.21

in *Tmc1*$^{dn/dn}$;*Cib2*$^{R186W/+}$;3.97± 0.18 in *Tmc1*$^{dn/dn}$;*Cib2*$^{R186W/R186W}$) were moderately reduced in the mutants.

Next, we carried out single channel recordings in hair cells at 40% of the distance along the cochlea from the low frequency end. Fig. S8I shows typical single channel events that were obtained with a 300 nm deflection. Single channel currents were significantly lower in OHCs from *Cib2*$^{R186W/R186W}$;*Tmc1*$^{dn/dn}$ mice compared to OHCs from *Cib2*$^{R186W/+}$;*Tmc1*$^{dn/dn}$ controls (3.91 ± 0.06 pA for *Cib2*$^{R186W/+}$;*Tmc1*$^{dn/dn}$; 3.40 ± 0.05 pA for *Cib2*$^{R186W/R186W}$; *Tmc1*$^{dn/dn}$, Fig. S8J). Taken together, our findings suggest that CIB2 affects the pore properties of the MET channel in hair cells. Since CIB2 is not a transmembrane protein, the effects are likely a secondary consequence of defects in CIB2 function.

## Discussion

We provide here evidence that CIB2 and CIB3 are auxiliary subunits of the MET channel in hair cells with important roles in regulating channel localization and function. Notably, CIB2 and CIB3 share striking structural similarity to NCS family members such as KChIP1 thus suggesting that CIB2 and CIB3 proteins are members of the NCS family. Consistent with this model, our findings reveal parallels between the CIB2/3-MET and $K_V$4-KChIP channel complex. In both instances, the respective NCS protein binds to the channel via a hydrophobic groove, regulates channel localization, and modulates channel properties, albeit in different ways. While KChIP proteins regulate channel inactivation kinetics, CIB2 affects channel resting $P_o$ without effects on adaptation. The latter conclusion is supported by the finding that a point mutation in *Cib2* linked to deafness (R186W) affects resting $P_o$ but not adaptation in hair cells from *Tmc1*$^{dn/dn}$;*Cib2*$^{R186W/R186W}$ mutant mice. The R186W mutation reduces but does not abolish binding of CIB2 to TMC proteins, indicative of structural changes in the protein interaction surface that affect ion channel function. These changes in protein:protein interactions might also explain the moderate changes in ion selectivity and single channel conductance observed in OHCs from *Tmc1*$^{dn/dn}$;*Cib2*$^{R186W/R186W}$ mutant mice. While our functional studies were carried out with CIB2, we show that CIB3 can compensate for the loss of CIB2 in OHCs. In addition, interactions between CIB2 and CIB3 with TMC1 and TMC2 are mediated by a conserved interface, suggesting that CIB3 regulates MET channel function in similar ways as CIB2. This is consistent with the observation that vestibular function is maintained in *Cib2* mutant mice, which, unlike cochlear hair cells, express both CIB2 and CIB3 (Patel et al., 2015; Riazuddin et al., 2012; Seco et al., 2016).

The structural resemblance of CIB3 with KChIP proteins and their mode of interaction with ion channel subunits is striking. CIB3 proteins form homodimers via a domain-swap mechanism, which are disrupted by TMC binding; similarly, KChIP1 forms homodimers, which are disrupted by binding to $K_V$4 (Pioletti et al, 2006). In CIB3 interactions with TMC1, the CIB3 C-terminal helix is displaced by binding to cytoplasmic elements of TMC1, thus enabling CIB3 to bind as monomers. Prior mapping studies (Giese et al., 2017) and our studies indicate that the N-terminal cytoplasmic tail of mammalian TMC1 – not included in the co-crystal structure reported here – also mediates CIB3-TMC1 interactions.

However, our immunoprecipitation results show that the cytoplasmic loop between predicted transmembrane domains 2 and 3 in TMC1, corresponding to the co-crystallized TMC1 peptide, provides high-affinity interactions. Notably, amino acids critical for interactions are conserved between CIB2 and CIB3 and between TMC1 and TMC2, suggesting that similar mechanisms drive interaction between CIB2/CIB3 and TMC1/TMC2. The overall similar mode of interaction among multiple NCS family proteins suggests that KChIPs, CIBs, and other NCS-family proteins derived from a common ancestor, and diversified in evolution to bind specific protein ligands. Our data also provide insights into mechanisms that determine binding specificity for NCS proteins. Amino acids critical for interactions of CIB2/3 with TMC1/2 are not conserved in CIB1 or KChIP1.

One major finding of our study is that CIB2 affects the localization of TMC1/2 to stereocilia. Defects in TMC1 and TMC2 localization are observed in mice with null alleles for *Cib2* or in mice carrying *Cib2* point mutations linked to deafness. The point mutations in *Cib2* linked to deafness do not affect amino acids that directly mediate interactions of CIB2 with the major TMC1 binding site between transmembrane domains 2 and 3. However, they perturb binding of CIB2 to TMC1, suggesting that the mutations might affect the overall CIB2 protein conformation to alter protein-protein interactions. Notably, while in *Cib2* null mutations the localization of both TMC1 and TMC2 to stereocilia of cochlear hair cells is abolished, some Cib2 mutations linked to deafness ($Cib2E^{64D/E64D}$ and $Cib2R^{186W/R186W}$) act as hypomorphs and affect TMC1 localization more severely compared to TMC2. Similar differential effects on the localization of TMC1 and TMC2 to stereocilia have been described for *Tmie* mutations (Cunningham et al., 2020). These data suggest that the transport or retention of the two TMC proteins depends on different mechanisms. We favor the hypothesis that CIB2, like TMIE, is not a transport protein per se but that incomplete assembly of an ion channel complex due to mutations in a critical component secondarily affects protein transport or retention.

The fact that TMC2 localization to stereocilia is not completely abolished in mice carrying several mutations linked to deafness allowed us to study effects of CIB2 mutations on channel properties. Our studies demonstrate that the $Cib2E^{64D/E64D}$ and $Cib2R^{186W/R186W}$ mutations affect the resting $P_o$ of the MET channel containing the TMC2 subunit that is present at early developmental stages in cochlear hair cells and into adulthood in vestibular hair cells. The effects are remarkable, where resting $P_o$ in mutant hair cells in high intracellular $Ca^{2+}$ is as high at positive holding potentials as the maximal values observed for wild-type hair cells in low intracellular $Ca^{2+}$. Resting $P_o$ is also nearly doubled in mutant hair cells compared to wild-type hair cells in low intracellular $Ca^{2+}$. However, the $Ca^{2+}$-dependent fold change in $P_o$ is similar at positive holding potentials for control and mutant OHCs, suggesting that the $Ca^{2+}$-dependent process may not be directly modulated by CIB2. Instead, CIB2 might act by an allosteric mechanism to stabilize the channel open state that is imparted by $Ca^{2+}$, a process that is affected by the R186W mutation.

How could CIB2 affect resting $P_o$? Studies in nematodes have shown that CALM-1, a nematode ortholog of CIB2 and CIB3, is required for TMC-dependent mechanosensation (Tang et al., 2020). CALM-1 binds to UNC-44, and it has been proposed that the CALM-1/UNC-44 complex mediates interactions with the cytoskeleton and may serve as a gating

spring (Tang et al., 2020). Perhaps, interactions of the transduction channel complex with the cytoskeleton is critical for setting resting $P_o$. Notably, the CIB2-E64D and CIB2-R186W mutant proteins are less tightly bound to TMC1/2, suggesting that a mechanical link would be weakened and tension in the spring reduced, not increased. However, several proteins might contribute to mediating interactions of the MET channel with the cytoskeleton, and a perturbation in the balance of these interactions might still lead to changes in the coupling of the MET channel to the cytoskeleton and affect the gating spring in complex ways. Alternatively, CIB2 might act independent of the cytoskeleton to affect TMC1 conformation. Further structural and biochemical studies will be necessary to distinguish between these possibilities.

Our studies with OHCs from *Cib2*$^{R186W/R186W}$ mutant mice demonstrate that adaptation is not affected by the mutation. This is consistent with recent findings regarding the regulation of resting $P_o$ and adaptation in mammals. Resting $P_o$ in hair cells responsive to low frequencies is commonly thought to depend on $Ca^{2+}$ entry through the MET channel to regulate adaptation (Fettiplace, 2017; Maoileidigh and Ricci, 2019). However, in mammalian cochlear hair cells, altering $Ca^{2+}$ entry or internal $Ca^{2+}$ buffering have little effect on adaptation, and resting $P_o$ is not simply a function of adaptation (Abecasis et al., 2002; Caprara et al., 2020; Peng et al., 2013; Peng et al., 2016). While others have questioned this conclusion (Beurg et al., 2015a; Corns et al., 2014), it is further supported by a recent study of hair cells carrying mutations in *Tmc1* and *Tmc2*, which show no strict correlation between $Ca^{2+}$ entry into hair cells and adaptation rate (Goldring et al., 2019). Our results are consistent with these findings and suggest that different molecular mechanisms contribute to the regulation of resting $P_o$ and adaptation in mammals.

The *Cib2*$^{R186W/R186W}$ mutation has moderate effects on the MET channel pore properties of TMC2-containing channels including effects on conductance and ion selectivity. It seems unlikely that CIB2 as a cytoplasmic protein directly contributes to the channel pore. We consider it more likely that these mild effects may be caused by indirect effects. CIB2 binds to a loop domain between TM2 and TM3 of TMC1, which is located within the cytoplasm next to the putative pore-forming TM domains (TM4–7) of TMC1/2. The R186W mutation is exposed to solvent in the extreme C-terminus of CIB2, which shows structural flexibility. Perhaps, the C-terminus of CIB2 is positioned close to the cytoplasmic face of the channel pore. A positively charged Arg amino acid might affect the flow of ions, a process that is affected by the R186W mutation that replaces Arg with a hydrophobic Trp residue. The R186W mutation also weakens interactions between CIB2 and TMC1/2. Since the R186W mutation is not within the interaction domain between CIB2 and TMC1/2, the mutation likely affects the CIB2 conformation and thus the structure of the CIB2/TMC1/2 complex. Allosteric effects on protein conformation could explain the mild effect of the R186W mutation on conductance and ion selectivity. Further structural studies of the protein complex containing channel components TMC1/2 and TMIE as well as the auxiliary subunit CIB2 will be important to test how different proteins contribute to the regulation of pore properties by mechanical force. In addition, it will be important to identify *Cib2* mutations that do not affect the localization of TMC1 to stereocilia to assess regulation of TMC1 by CIB2.

# STAR★METHODS

## Lead contact

Ulrich Müller. The Solomon H. Snyder Department of Neuroscience, Johns Hopkins University School of Medicine, Baltimore, MD 21205, USA.

umuelle3@jhmi.edu

443-287-4762

## RESOURCE AVAILABILITY

**Lead Contact—**Further information and requests for resources and reagents should be directed to and will be fulfilled by the Lead Contact, Ulrich Mueller (umuelle3@jhmi.edu).

**Materials Availability—**Newly generated materials such as genetically modified mouse lines are available to qualified researchers upon request and after providing a signed MTA agreement.

**Data and Code Availability—**This study did not generate any code. The accession number for the coordinates and structural factors for *homo sapiens* CIB3, *homo sapiens* CIB3 EK150QH, and the complex of *homo sapiens* CIB3 with *mus musculus* TMC1 peptide reported in this paper are PDB: 6WU5, PDB: 6WU7, and PDB: 6WUD, respectively.

## EXPERIMENTAL MODEL AND SUBJECT DETAILS

**Mouse strains—**All animal experiments were approved by the Institutional Animal Care and Use Committee at Johns Hopkins University School of Medicine (#M016M271). Mice were maintained on a 14 hr. light/10 hr. dark cycle. Both male and female mice were used, and no obvious differences between the sexes were noted. All mice were group-housed in pathogen-free facilities with regulated temperature and humidity and given *ad libitum* access to food and water. All of the mice used were seemingly free of infection, health abnormalities, or immune system deficiencies. None of the mice used had been used for previous experiments. For injectoporation, immunostaining and electrophysiological recording, mice were used at ages postnatal day 2 (P2) to P8. For ABR experiments, mice were ages 4–6 weeks. Mice from each strain were used as wild-type, heterozygous, or homozygous for the genetic modification and details are provided in the paper where appropriate. Controls for experiments were wild-type or heterozygous litter-mates.

Mice with loss-of-function alleles in *Cib2* (*Cib2* $^{tm1a}$) were generated from sperm obtained from EUCOMM. CRISPR/Cas9 technology was used to generate *Cib2-E64D, Cib2-I123T, Cib2-R186W* mice. Exons were analyzed for potential sgRNA target sites using the website CRISPOR (crispor.tefor.net). Target sites were chosen based on proximity to desired genomic region and minimal number of predicted off-target sites. Target specific crRNA and tracrRNA were ordered from Integrated DNA Technologies (IDT). For point mutations, ssDNAs containing desired mutations were designed containing 60 bp homology arms flanking the region of interest. ssDNAs also included silent mutations to PAM sites to prevent excessive cleavage by CAS9 after integration. Pronuclear injection of one-cell

C57BL/6J embryos (Jackson Laboratories) was performed by the JHU Transgenic Core using standard microinjection techniques using a mix of Cas9 protein (30ng/ul, PNABio), tracrRNA (0.6μM, Dharmacon), crRNA (0.6μM, IDT) and ssDNA oligo (10ng/ul, IDT) diluted in RNAse free injection buffer (10 mM Tris-HCl, pH 7.4, 0.25 mM EDTA). Injected embryos were transferred into the oviducts of pseudopregnant ICR females (Envigo). Offspring was screened using PCR and sequencing to determine presence of point mutations. Founder mice were bred with C57BL/6J mice (RRID:IMSR JAX:000664) for at least two generations and offspring were screened to verify germ-line transmission of mutations.

**Genetic modifications for each strain:** *Cib2-E64D: 5'-GAG-3'* encoding E64, was mutated to 5'-*GAC-3'*, encoding D64 of mouse *Cib2. Cib2-I123T: 5'-ATC-3'* encoding I123, was mutated to 5'-*ACC-3'*, encoding T123, of mouse *Cib2.*

*Cib2-R186W: 5'-CGA-3'* encoding R186, was mutated to 5'-*TGG-3'*, encoding W186, of mouse *Cib2.*

**Cell Lines—**The HEK293 (ATCC# CRL-1573), HAP-1 (Horizon #C631) and COS-7 (ATCC#CRL-1651) cell lines were used for heterologous expression. Cells were grown at 37°C, 5% $CO_2$ in 1X DMEM+Glutamax (Gibco) containing 10% Fetal Bovine Serum and 1X Antibiotic-Antimycotic (Gibco). Cells used in experiments were passaged a maximum of twenty times.

## METHOD DETAILS

**Auditory Brainstem Response (ABR) and Distortion Product Otoacoustic Emissions (DPOAE)—**ABR measurements were performed as previously described (Cunningham et al., 2020). In short, 4–6 weeks old mice were anesthetized with Ketamine (100 mg/kg) and Xylazine (20 mg/kg) via intraperitoneal (i.p.) injections and placed on a heating pad inside of a sound attenuating chamber. The animal's body temperature was closely monitored throughout the test session using a rectal temperature probe. ABRs were recorded from the scalp via differential recording by placing subdermal platinum needle electrodes (E2, Grass Technologies, West Warwick, RI) on the left pinna (inverting), vertex (non-inverting), and on leg muscle (ground). ABR stimuli generation and signal acquisition were controlled by a custom MATLAB program interfacing TDT System 3 and PA5 Programmable Attenuator (Tucker-Davis Technologies (TDT), Alachua, FL). ABR stimuli consisted of clicks and 5-ms tone pips of varying frequencies (8, 12, 16, 24, 32 kHz) and presented at a rate of 20/s. ABR stimuli were delivered through a free-field speaker (FD28D, Fostex, Tokyo, Japan), placed 30 cm away from the animal's head. Stimuli were presented in descending sound levels from maximum speaker output level in 5–10 dB increments until ABR signals were no longer discernable from the background. Responses were amplified 300,000 × (ISO-80, Isolated Bio-Amplifier, World Precision Instruments, Sarasota, FL), band pass filtered 300–3000 Hz (Krohn-Hite Model 3550, Krohn-Hite Corporation, Avon, MA), digitized (RX6 Multifunction Processor, TDT), and averaged over 300 presentations. Threshold was determined statistically based on ABR input/output function and defined

as the sound level at which the peak-to-peak ABR signal magnitude was two standard deviations above the average background noise level.

DPOAE measurements were conducted in a separate session from ABR testing. Mice were anesthetized (i.p.) with Ketamine (100 mg/kg) and Xylazine (20 mg/kg) and placed on a heating pad inside of a sound attenuating chamber. DPOAEs were measured from the ear canal near the tympanic membrane, using a DPOAE probe system (ER-10C, Etymotic Research Inc, Elk Grove Village, IL), containing two built-in sound speakers and low noise microphone. DPOAE stimulus frequencies were generated by TDT system 3 RX6 Multifunction Processor (TDT) and custom MATLAB-based program and routed through ER-10C DPOAE Driver-Preamp (Etymotic Research Inc) and delivered to the ear canal via ER-10C DPOAE probe system. The DPOAE probe was tightly fitted into the ear canal using a miniature ear tip to form a closed-field acoustic system. In-ear pressure calibration was performed before each test. DPOAE signals consisted of two primary frequencies, $f_1$ and $f_2$, at a ratio of $f_2/f_1 = 1.2$ where $f_1 < f_2$. For each primary frequency pair, $f_1$ tone level ($L_1$) was presented 10 dB SPL higher than $f_2$ tone level ($L_2$), such that $L_1 - L_2 = 10$ dB. For each $f_2$ frequency (8, 12, 16 kHz), $L_2$ was incremented from 10 to 55 dB SPL in 5 dB steps. DPOAE responses were averaged and the cubic distortion product ($2f_1$-$f_2$) component amplitude was determined. DPOAE threshold was calculated manually offline by interpolating $2f_1$-$f_2$ amplitude function, in which threshold was defined as the sound level where $2f_1$-$f_2$ signal level was two standard deviations above the noise floor.

ABR and DPOAE data analyses were performed offline. Figures were generated using Origin Pro 7.5 (Origin Lab, Northampton, MA). All data is shown as mean ± SEM, unless otherwise noted.

**Injectoporations of cochlear hair cells—**Injectoporation experiments were used to express exogenous DNA in cochlear hair cells as previously described (Cunningham et al., 2017; Xiong et al., 2012; Xiong et al., 2014; Zhao et al., 2014; Zhao et al., 2016). Briefly, the Organ of Corti was isolated from P2–3 wild-type and mutant mice and cultured as explants in 1X DMEM/F12 media containing 1.5 μg/ml ampicillin. Plasmid DNA constructs (1 μg/mL) were injected in explants using glass pipettes (2 μm diameter) between rows of outer hair cells. Explants were electroporated with four pulses at 60 V (15 msec pulse length, 1 sec inter-pulse intervals, ECM 830 square wave electroporator; BTX). After electroporation, culture media was replaced with DMEM/F12 media containing 10% fetal bovine serum. Explants were incubated for 1–2 days at 37°C, 5% $CO_2$ before electrophysiological recording and/or immunostaining (see details below).

**Electrophysiology—**MET current recording was performed following our published procedures (Cunningham et al., 2020; Xiong et al., 2012; Xiong et al., 2014). During recording, apical perfusion was used to perfuse artificial perilymph (in mM): 144 NaCl, 0.7 $NaH_2PO_4$, 5.8 KCl, 1.3 $CaCl_2$, 0.9 $MgCl_2$, 5.6 glucose, and 10 H-HEPES, pH 7.4. Borosilicate glass pipettes (Sutter, CA) were pulled with a P-2000 pipette puller (Sutter, CA), and polished with a MF-930 microforge (Narishige, Japan) to resistances of 2–3 MΩ. Hair bundles were mechanically deflected with a glass probe mounted on a piezoelectric stack actuator (Thorlab, Newton, NJ) or Fluid Jet from a glass pipette that was produced

by a 27-mm-diameter piezoelectric disc. For glass probe stimuli, the actuator was driven by voltage steps that were low-pass filtered at 10 KHz with a 900CT eight-pole Bessel filter (Frequency Devices) to diminish the resonance of the piezo stack. For Fluid Jet, sinusoids (40 Hz) were applied and filtered at 1.0 kHz. Whole-cell recordings were carried out and currents were sampled at 100 KHz with an EPC 10 USB patch-clamp amplifier (HEKA, Germany). To record macroscopic currents, the patch pipette was filled with intracellular solution (in mM): 140 KCl, 1 $MgCl_2$, 0.1 EGTA, 2 Mg-ATP, 0.3 Na-GTP and 10 H-HEPES, pH 7.2. In some experiments, KCl was replaced by CsCl, intracellular $Ca^{2+}$ buffer by 1mM or 10mM BAPTA. Cells were voltage-clamped at −74mV (unless otherwise noted). Uncompensated series resistance was less than 5 MΩ. For single-channel recordings, we followed our published procedures (Xiong et al., 2012). To measure single-channel currents, hair cells were held at −80 mV. The intracellular solution consisted of (in mM) 140 CsCl, 1 $MgCl_2$, 1 EGTA, 2 Mg-ATP, 0.3 Na-GTP and 10 H-HEPES, pH 7.2. After whole cell configuration, hair cells were briefly treated with $Ca^{2+}$ free solution (in mM): 144 NaCl, 0.7 $NaH_2PO_4$, 5.8 KCl, 5 EGTA, 0.9 $MgCl_2$, 5.6 glucose, and 10 H-HEPES, pH 7.4. A 300nm deflection was applied to the bundle by a stiff probe and low-pass filtered at 1KHz. Single channel currents were recorded and offline filtered at 1KHz for further analysis. The events with significant plateau of open status were chosen for amplitude analysis. For reversal potential measurements, the external solution consisted of (in mM) 100 CaCl2, 20 N-methylglucamine, 6 Tris, 10 Glucose, pH 7.4. The internal solution consisted of (in mM) 135 CsCl, 3 MgATP, 10 Tris phosphocreatine, 1 EGTA. The liquid junction potential for the solutions in this study was corrected.

**Whole-mount and explant immunohistochemistry and imaging—**Whole mount cochleas or explants after injectoporation from postnatal wildtype and mutant mice were dissected, fixed, and immunostained as described (Cunningham et al., 2020; Xiong et al., 2012; Xiong et al., 2014). Briefly, for whole mounts, temporal bones were removed from the skull in 1x HBSS containing 0.1 mM $CaCl_2$. Openings were made in the bony cochlear shell at the apex and through the oval and round windows. Temporal bones were incubated in 1x HBSS containing 4% PFA and 0.1 mM $CaCl_2$ for 30 minutes at RT with gentle agitation. The bony cochlear shell was removed after three washes in PBS. The Organ of Corti was separated from the modiolus and collected in PBS. Reissner's membrane and the Tectorial membrane were dissected away. For explants, dishes containing explants were incubated with 1x HBSS containing 4% PFA and 0.1mM $CaCl_2$ for 30 minutes at RT, and then washed three times with PBS. The Organ of Corti was permeabilized in PBS containing 0.5% Triton for 30 minutes at RT with agitation. After permeabilization, the tissue was blocked in PBS containing 10% Goat Serum (GS) for 4–6h at RT. The tissue was then incubated in PBS containing 5% GS and primary antibodies overnight at 4°C. The tissue was then washed three times in PBS and incubated for 1 hour at RT in PBS containing 5% GS, secondary antibodies (1:5000 dilution), and fluorescently-conjugated Phalloidin to label stereocilia (Life Technologies, Phalloidin 555, 1:1000). After secondary antibody incubation, the tissue was washed three times and mounted using ProLong Gold (Invitrogen). Tissues were imaged on a widefield fluorescence deconvolution microscope with 100x lenses (Deltavision, GE Life Sciences).

Primary antibodies were as follows: rabbit anti-HA (1:200, Cell Signaling, RRID: RRID:AB_1549585), rabbit anti-MYC (1:200, Cell Signaling, RRID:AB_490778). Secondary antibodies were as follows: Goat anti-rabbit IgG F(ab')2, Alexa Fluor 488 (1:5000, Invitrogen, RRID:AB_2534114). The CIB2 antibody was generated as follows: Full length murine CIB2 was fused to a His-tag in the pET28a expression vector and expressed as protein in bacteria. His-tagged CIB2 proteins were purified by binding to Ni-beads. Rabbits were immunized with full-length CIB2 proteins at Covance. CIB2 antibodies were affinity purified against full-length CIB2 protein coupled to Sepharose CL4B. We verified that the purified antibody labeled hair cells from wild-type but not from *Cib2*$^{-/-}$ mice (data not shown).

Imaris software (Bitplane, Inc) was used to quantify expression levels of TMC1-HA and TMC2-MYC in hair bundles. For comparison, all images were acquired with similar exposure parameters. First, the outer hair cell bundle was reconstructed in three dimensions based on phalloidin staining. Second, TMC1-HA or TMC2-MYC puncta within the bundle area defined by this reconstruction were identified with significant high intensity as shown in Fig. 2D. Within each bundle, the mean voxel intensities of all positive puncta were summed to create a measure of expression level for that bundle.

**Co-immunoprecipitation and western blotting—**Co-immunoprecipitations were performed as described (Cunningham et al., 2020; Cunningham et al., 2017; Zhao et al., 2014; Zhao et al., 2016). Briefly, HEK293 cells were transfected with plasmids using Lipofectamine 3000 (ThermoFisher). After 36 hours, cells were lysed using a modified RIPA buffer containing 150 mM NaCl, 50 mM Tris (pH 8.0), 1% NP-40, 0.5% Sodium Deoxycholate, 0.1% Sodium Dodecyl Sulfate (SDS) and a Roche Complete Protease Inhibitor Tablet. After lysis, lysates were rotated for 30 minutes at 4°C followed by centrifugation at 15000 rpm for 20 minutes at 4°C. At this point, 10% of the lysate was set aside for use as an input control. The rest of the lysate was immunoprecipitated for 1 hour at 4°C using EZ View Red anti -HA Affinity Gel (Sigma-Aldrich Cat# E6779–1ML) or EZ View Red anti-c-MYC Affinity Gel (Sigma-Aldrich Cat# E6654–1ML). After immunoprecipitation, the affinity gel was washed three times with IP buffer containing 150 mM NaCl, 50 mM Tris (pH 8.0), 1% NP-40. After discarding all the buffer, the immunoprecipitated proteins were eluted with 1x SDS Sample Buffer (Bio-Rad) containing BME (Bio-Rad). Eluted immunoprecipitated protein was run in parallel with input lysate on Novex™ WedgeWell™ 4 to 20%, Tris-Glycine, 1.0 mm, Mini Protein Gels (Life Technologies) and transferred to PVDF membranes (Sigma) for 2.5 hour with 250 mA current at 4°C using the Mini Blot Module (Bio-Rad) containing Bio-Rad transfer buffer (Bio-Rad) with 20% Methanol. Membranes were blocked for 1 hour with 5% Blotting Grade Blocker Non-Fat Dry Milk (Bio-Rad) in 1X PBST (containing 20 mM Tris-HCl pH 7.5, 150 mM NaCl and 0.05% Tween-20). Membranes were incubated with primary antibodies (see below) in 5% Milk in 1X PBST at 4° C overnight. After primary antibody incubation, membranes were washed three times with 1X PBST, followed by incubation for 1 hour at RT in 5% Milk containing secondary antibodies (see below) in 1X TBST. Membranes were washed three times in 1X TBST and then imaged with Clarity Substrate (Bio-Rad) on a G-Box ECL imager (Syngene). Quantification of CoIP experiments was done using ImageJ

and Graph-Pad Prism 6. Western blot band intensity values were obtained using ImageJ for IP bands and whole cell lysate bands for both IP and CoIP proteins. For each experiment, CoIP intensity values were normalized for expression and immunoprecipitation efficacy and divided by controls to generate relative CoIP Intensity values. Mean relative CoIP intensity values were calculated by combining relative values for each construct across independent experiments. For each construct, a mean value was calculated, and statistical significance relative to control constructs were evaluated using a Students' t-test.

Primary antibodies were as follows: rabbit anti-MYC (1:500, Cell Signaling), rabbit anti-HA (1:500, Cell signaling), mouse anti-MYC (1:500, Cell Signaling) and mouse anti-HA (1:500, Cell signaling).

Secondary antibodies were Veriblot (1:5000, Abcam) and Veriblot anti-mouse (1:5000, Abcam).

**Immunofluorescence analysis of transfected cells—**Cells (HAP-1 and HEK293) were plated and cultured to 70–90% in six-well dishes, followed by transfection with plasmids using Lipofectamine 3000 (ThermoFisher). 24 hours after transfection, cells were trypsinized, removed from dishes and plated at a lower density on Poly-L-Lysine-treated coverglass. After 24 hours, coverslips containing cells were fixed for 10 min with 2% PFA, washed with PBS and permeabilized for 5 min with 0.1% Triton. Coverslips were blocked for 1 hour with 10% Goat Serum (Millipore) in PBS, followed by incubation with primary antibodies in blocking solution overnight at 4°C. The coverslips were washed with PBS, incubated with secondary antibodies for 1 hr at RT, followed by additional PBS washes. Finally, coverslips were briefly dipped in $ddH_2O$ and mounted on slides with Prolong Gold. Cells on coverslips were imaged were on a widefield fluorescence deconvolution microscope with 60x lenses (Deltavision, GE Life Sciences).

Primary antibodies were as follows: rabbit anti-CIB2 (1:1000, Mueller Lab described above) and mouse anti-HA (1:500, Cell signaling RRID:AB_10691311).

Secondary antibodies were Goat anti-rabbit IgG F(ab')2, Alexa Fluor 555 (1:10000, Invitrogen, RRID:AB_2535851), and Goat anti-mouse IgG F(ab')2, Alexa Fluor 647 (1:10000, Invitrogen, RRID:AB_2535806). In some experiments, Phalloidin conjugated to Alexa Fluor 555 (1:1000) was used as a marker for actin and the cell surface.

For quantification of surface vs internal fluorescence, Z stacks were collected of transfected cells encompassing the entire cell. Individual image planes were analyzed where the surface was in maximal focus (determined by TMIE-HA localization or Phalloidin staining). Fluorescent intensity values for TMC1 or TMIE were obtained from unique regions of interest (ROIs) from selected regions of the cell surface and internal cell body using Deltavision Elite software. For each cell, ROIs were averaged for the surface and internal locations, respectively, and then a ratio of surface/internal fluorescence was calculated.

**Protein preparation—**Wild-type CIB3 and CIB3 mutant EK150QH were sub-cloned into a pET-28a vector, while TMC1 was sub-cloned into a pET-15b vector. The recombinant plasmids were transformed into E. coli strain BL21(DE3)-CodonPlus-RIPL and used to

overexpress His6-tag fusion proteins. CIB3:TMC1-peptide complexes were co-expressed by transformation with both plasmids. Cells were induced with 1 mM IPTG, and allowed to incubate for an additional 16–20 hours at 16°C. After incubation, the cells were harvested by centrifugation, suspended in 20 mM Tris-HCl pH 8.0, 500 mM NaCl, and 25 mM imidazole, and lysed by sonication. The lysate was centrifuged at 16,000 x g for 35 min to remove cell debris. The supernatant was loaded twice onto a Ni-NTA column (Qiagen) pre-equilibrated with lysis buffer. Target proteins were eluted with 20 mM Tris-HCl, pH 8.0, 150 mM NaCl, and 250 mM imidazole. Recombinant proteins were further purified with a Superdex-200 gel-filtration column (GE Healthcare). The purified proteins were concentrated to 15 mg/ml in 20 mM Tris, pH 8.0, 150 mM NaCl, 5mM $Ca^{2+}$ for crystallization. Mutations were introduced with QuikChange PCR (Stratagene).

**Crystallization, data collection and structure determination—**Initial crystallization screening was performed with 96 conditions using a Mosquito Crystallization Robot by the vapor diffusion method in sitting drops containing 0.1ul of protein and 0.1ul of reservoir solution at 20°C. Screens were imaged by a Formualtrix R1–1000 imaging robot. CIB3 wild-type crystals were grown in 20 mM Tris pH 7.5, 1.5M lithium sulfate, and 200 mM sodium thiocyanate; The CIB3-E150QK151H crystals were grown in 20 mM Tris pH 7.5, 10% PEG 8000, 200 mM Calcium Acetate. CIB3:TMC1 peptide (298–352aa) crystals were grown in 20mM Tris pH 8.0, 25% PEG 3350, and 200 mM $MgCl_2$. The crystallization drop in all experiments contained 5mM $CaCl_2$. All crystals were picked from hanging drops in 24-well optimization plates. For X-ray data collection, the crystals were flash frozen in liquid nitrogen with cryoprotectant prepared from the reservoir solution supplemented with 25% glycerol.

Diffraction data were collected with 1.46 Å (wt CIB3, CIB3 EK150QH) or 1.77 Å (CIB3:TMC1) X-rays at NE-CAT beamline 24-ID-C (Advanced Photon Source, Argonne National Laboratory) and processed with the XDS and AIMLESS (Evans and Murshudov, 2013; Kabsch, 2010). All datasets were collected at wavelengths that were suitable for Bijvoet difference Fourier maps to visualize calcium ions. Structures were solved by molecular replacement using PHASER, and iterative model building and refinement were carried out in COOT and PHENIX, respectively (Adams et al., 2004; Emsley and Cowtan, 2004). A cross validation ($R_{free}$) test set consisting of 5% of the data was used throughout the refinement processes.

**Homology Modeling—**The homology model of CIB2 was generated using the I-TASSER server, using the structure of CIB3 from the CIB3:TMC1-peptide co-crystal structure

**DNA constructs and plasmids—**DNA constructs were generated as described below. All constructs were sequence-verified.

For electrophysiology, cDNAs encoding CIB1, CIB2, CIB3, KChIP1, TMC1, TMC2 and their mutants were cloned into pCAGEN or pCAGEN-IRES-GFP. For CoIP and injectoporation to determine protein localization of CIB1, CIB2, CIB3, KChIP1, TMC1, TMC2 and their mutants, we used the pN3 vector (Zhao et al., 2014). All constructs were generated by PCR-cloning using primers containing restriction enzyme sites, epitope

tags, and extra nucleotides to allow for restriction digest. Mutations were introduced with QuikChange PCR (Stratagene).

**Primers:** Clone MsCib1 into a pRK5 vector primer

5’ CTACGCTTCTAGAACTAGTGGATCCATGGGGGGCTCGGGCAGTC 3’ containing a BamH1 restriction site; 5’ GAGGTCGACGGTATCGATTACAGGACAATCTTAAAGGAGCTG 3’ containing a SalI restriction site. The construct was cloned into the Prk5 derived vector in which HA tag was inserted before the BamH1 restriction site. All mscib2, mscib3 and mskchip1 are clone into the vector.

Clone MsCib2 into a pRK5 vector primer

5’ CTACGCTTCTAGAACTAGTGGATCCATGGGGAACAAGCAGACCATC 3’ containing a BamH1 restriction site; 5’ GAGGTCGACGGTATCGATAAGCTCAGATTCGAATGTGGAAGGTG

3’ containing a SalI restriction site.

Clone MsCib3 into a pRK5 vector primer

5’ CTACGCTTCTAGAACTAGTGGATCCATGGGCAACAAGCAGACTGT 3’ containing a BamH1 restriction site; 5’ GAGGTCGACGGTATCGATAAGCtcaGATGCGGATGTGGAAGG 3’ containing a SalI restriction site.

Clone MsKchip1 into a pRK5 vector primer

5’ CTACGCTTCTAGAACTAGTGGATCCATGGGGGCCGTCATGGG 3’ containing a BamH1 restriction site; 5’ GAGGTCGACGGTATCGATTACATGACATTTTGGAACAGCTGTAG 3’ containing a SalI restriction site.

Clone human Cib3 to pET28a

5’ CGAAAACCTGTATTTTCAGGGCATGGGCAACAAGCAGACAG 3’ and 5’ GACGGAGCTCGAATTCGGATCCTTAGATGCGGATGTGGAAGGTG 3’ using NEBuilder® HiFi DNA Assembly Master Mix(Biorad)( Cat#: E2621S) to clone human cib3 to pET28a; The human Cib3 E150QK151H mutation primer, 5’ GTGACCCTGGTCTGTCAACACGTGCTGGATGAAGCA 3’ and 5’ GTGTTGACAGACCAGGGTCACTTCCTCAGC 3’ using QuikChange II XL site-directed mutagenesis Kit (Agilent)( Cat#: 200521).

Clone MsTmc1(298–352aa) to pET15b

5’ CCGCGCGGCAGCCATATGGGTGGTGGCGATGACAAC 3’ and 5’ GATAGGCTTACCGCTACCACTTCAGATGTTCTCCTCCACCTGTG 3’ using NEBuilder® HiFi DNA Assembly Master Mix.

Other primers for Cib2, Cib3, Tmc1 mutation

MsTmc1D100–105

5’ CAAATGATCGCTACTAAAATGGAGAAGAAAATTG 3’ and

5’ TTTTCTTCTCCATTTTAGTAGCGATCATTTGTCT 3’

MsTmc1D108–111

5’ ATGTAAACCTTGGAAAGAAGTTCTCAAGGAAGCA 3’ and

5’ TTCCTTGAGAACTTCTTTCCAAGGTTTACATTTG 3’

MsTmc1D114–121

5’ GAAGAAAATTGAAGTTAGTGAGAATGAAGGCG 3’ and

5’ CTTCATTCTCACTAACTTCAATTTTCTTCTCC 3’

MsTmc1D125–129

5’ TTTGTGAGTGAGAATAAAGGAAAGGGAAAGAAG 3’ and

5’ CTTTCCCTTTCCTTTATTCTCACTCACAAATTT 3’

MsTmc1D130–134

5’ GGCGCTCTTGGGAAGTGGTTTGCATTTAAG 3’ and

5’ AAATGCAAACCACTTCCCAAGAGCGCCTTC 3’

MsTmc1D161–165

5’ AACTTCAAAGCGGCTAACAAAATCAAGGCAATTG 3’ and

5’ TTGCCTTGATTTTGTTAGCCGCTTTGAAGTTCTC 3’

MsTmc1D166–169

5’ GCGTCCCATGGGAAGCAATTGAAAGTCAGTTTG 3’ and

5’ ACTGACTTTCAATTGCTTCCCATGGGACGCAAG 3’

MsTmc1D171–175

5’ AAACAAAATCAAGGCAGGTTCCTCAGTGGCCTC 3’ and

5’ GCCACTGAGGAACCTGCCTTGATTTTGTTTTCC 3’

MsTmc1D176–181

5’ AATTGAAAGTCAGTTTTACTTCCTGTTCCTCAGG 3’ and

5’ GAGGAACAGGAAGTAAAACTGACTTTCAATTGCC 3’

MsTmc1D182–186

5’ TCCTCAGTGGCCTCGAGGTGGATGTACG 3’ and

5’ CGAGGCCACTGAGGAACCAAACTGACTT 3’

MsTmc1D187–190

5’ GTACTTCCTGTTCCTCGGCGTCAACATG 3’ and

5’ GAGGAACAGGAAGTACGAGGCCACTGAG 3’

MsTmc1D289–294

5’ CCTGGTTGTCCTCAAAGGTGACGATGGTGGTG 3’ and

5’ CACCATCGTCACCTTTGAGGACAACCAGGAAG 3’

MsTmc1D295–297

5’ CGATGACCAAAAATATTGGTGGTGGCGA 3’ and

5’ AATATTTTTGGTCATCGCTTTGAGGACAAC 3’

MsTmc1D289–300

5’ GCGATGACCAAAAATATTTTGGTGACGATGGTGGT 3’ and

5’ ACCACCATCGTCACCAAAATATTTTTGGTCATCGC 3’

MsTmc1D298–303

5’ AAATATTGGTGACGATACTTTCAACTTCAGCTGG 3’ and

5’ GCTGAAGTTGAAAGTATCGTCACCAATATTTTTG 3’

MsTmc1D305–307

5’ TGGCGATGACAACACTAGCTGGAAGGTGTT 3’ and

5’ AGTGTTGTCATCGCCACCACCATCGTCAC 3’

MsTmc1D309–312

5’ ACACTTTCAACTTCAGCTGTAGCTGGGACTAT 3’ and

5’ GCTGAAGTTGAAAGTGTTGTCATCGCCACC 3’

MsTmc1D316–319

5’ GGAAGGTGTTCTGTAGCGGTAACCCTGAAAC 3’ and

5’ GCTACAGAACACCTTCCAGCTGAAGTTGAAAG 3’

MsTmc1D323–329

5’ AGCCGACAACAAGTTTAACTCTATCACGATG 3’ and

5’ AAACTTGTTGTCGGCTGTTTCAGGGTTACC 3’

MsTmc1D336–339

5’ TCTATCACGATGAACGCCATCATAGAAGAGAG 3’ and

5’ TCTTCTATGATGGCGTTCATCGTGATAGAGTT 3’

MsTmc1D340–344

5’ AACTTTAAGGAAGCCGCCGCACAGGTGGAG 3’ and

5’ CACCTGTGCGGCGGCTTCCTTAAAGTTCAT 3’

MsTmc1D349–352

5’ GCCGCACAGGTGCACCTCATCAGATTTCTG 3’ and

5’ AAATCTGATGAGGTGCACCTGTGCGGCTCT 3’

MsTmc1–1-181

5’ CTCAGTGGCCTCGTAATTCCTGTTCCTCAG 3’ and

5’ TTACGAGGCCACTGAGGAACCAAACTGAC 3’

MsTmc1–1-210

5’ CAGCCTCATCATGTTACCGGAGTACCTCTGA 3’ and

5’ CGTACGGTAAACCTCAGAGGTACTCCGGTAA 3’

MsTmc1–1-396

5’ CTGACACCCTTGGGTAGTGGGAAAAAAATG 3’ and

5’ TACCCAAGGGTGTCAGGATCTTGCTGGG 3’

MsTmc1–71-396

5’ GCGGAAGAAGAAGAAGAAATTGATGGATCCTGACACCCTTGGG 3’ and

5’ CCCAAGGGTGTCAGGATCCATCAATTTCTTCTTCTTCTTCCGC 3’

MsTmc1–81-396

5’ GAGGAATTAGAACGGTTAGATCCTGACACCCTTGGG 3’ and

5’ CCCAAGGGTGTCAGGATCTAACCGTTCTAATTCCTC 3’

MsTmc1–91-396

5’ GATGAGAATAGACAAATGGATCCTGACACCCTTGGG 3’ and

5’ CCCAAGGGTGTCAGGATCCATTTGTCTATTCTCATC 3’

MsTmc1–100-396

5’ GTCAAATGTAAACCTTGGGATCCTGACACCCTTGGG 3’ and

5’ CCCAAGGGTGTCAGGATCCCAAGGTTTACATTTGAC 3’

MsTmc1–127-396

5’ GCTCTTGGGAAAGGAAAGATCCTGACACCCTTGGG 3’ and

5’ CCCAAGGGTGTCAGGATCTTTCCTTTCCCAAGAGC 3’

MsTmc1–1-375

5’ TGGTGCAAGTGGATACTAAATCTTTTGGGCTGT 3’ and

5’ TTAGTATCCACTTGCACCAAGTGTGAGGAACA 3’

MsTmc1-M105016A

5’ CTGTCAAATGTAAACCTGCGGCAATGGAGAAGAAAATT 3’ and

5’ TGCCGCAGGTTTACATTTGACAGTAGCGATCATTTGT 3’

MsTmc1-M109110111A

5’ AACCTTGGAAAATGGAGGCGGCAGCTGAAGTTCTCAAGGAA 3’ and

5’ GCTGCCGCCTCCATTTTCCAAGGTTTACATTTGACAGTAGC 3’

MsTmc1-M114115116A

5’ GAGAAGAAAATTGAAGTTGCCGCGGCAGCAAAGAAATTTGTGA 3’ and

5’ GCCGCGGCAACTTCAATTTTCTTCTCCATTTTCCAAGGTT 3’

MsTmc1-M120121A

5’ CTCAAGGAAGCAAAGAAAGCTGCGAGTGAGAATGAAGG 3’ and

5’ GCAGCTTTCTTTGCTTCCTTGAGAACTTCAATTTTCTTC 3’

MsTmc1-M305306307A

5’ TGGCGATGACAACACTGCCGCCGCCAGCTGGAAGGTGT 3’ and

5’ GCGGCGGCAGTGTTGTCATCGCCACCACCATCGTCAC 3’

MsTmc1-M309310311A

5’ ACACTTTCAACTTCAGCGCGGCGGCGGCCTGTAGCTGGGAC 3’ and

5’ GCCGCCGCCGCGCTGAAGTTGAAAGTGTTGTCATCGCCAC 3’

MsTmc1-M315316317318A

5’ GCTGGAAGGTGTTCTGTGCCGCGGCCTATCTGATTGGTAACC 3’ and

GCCGCGGCACAGAACACCTTCCAGCTGAAGTTGAAAGTGT 3’

MsTmc1-M326327328329A

5’ GTAACCCTGAAACAGCCGCCGCCGCGGCTAACTCTATCACGATG 3’ and

5’ GCCGCGGCGGCGGCTGTTTCAGGGTTACCAATCAGATAGTCC 3’

MsTmc1-M336337338A

5’ TAACTCTATCACGATGAACGCTGCGGCAGCCATCATAGAAGAG 3’ and

5’ GCCGCAGCGTTCATCGTGATAGAGTTAAACTTGTTGTCGG 3’

MsTmc1-M340341342343344A

5’ TGAACTTTAAGGAAGCCGCCGCAGCAGCGGCAGCCGCACAGG 3’ and

5’ GCCGCTGCTGCGGCGGCTTCCTTAAAGTTCATCGTGATAGAGTTAA 3’

MsCib2N68Q

5’ CCGGAGCTCCGGGAGCAACCCTTCAAAGAGAG 3’ and

5’ TTGCTCCCGGAGCTCCGGCATCTGAATGATGAG 3’

MsCib2I114F

5’ GCAAACTATGCCTTCAAGTTCTATGACTTCAACAC 3’ and

5’ ACTTGAAGGCATAGTTTGCCTTGAGCTCCCG 3’

MsCib2T131L

5’ GTAAAGAAGACTTAGAGATGCTGCTGGCCCGAC 3’ and

5’ AGCATCTCTAAGTCTTCTTTACAGATGAAATTGTCAG 3’

MsCib2L140R

5’ CTCACCAAGTCTGAGAGGGAAGAGGATGAGG 3’ and

5’ CTCTCAGACTTGGTGAGTCGGGCCAGC 3’

MsCib2V148F

5’ GATGAGGTAGTGCTTTTTTGTGACAAAGTCATTG 3’ and

5’ AAAAAGCACTACCTCATCCTCTTCCAACTCAG 3’

MsCib2V152F

5’ CTTGTGTGTGACAAATTCATTGAAGAGGCTG 3’ and

5’ ATTTGTCACACACAAGCACTACCTCATCC 3’

MsCib3N68Q

5’ CCAGAGCTGAAGGATCAACCTTTCCGCCAG 3’ and

5’ TTGATCCTTCAGCTCTGGCATGCTGCCAAT 3’

MsCib3I114F

5’ CTACTATGCCTTCAAGTTTTATGACTTCAACAATG 3’ and

5’ ACTTGAAGGCATAGTAGGCCTTCAGGTCC 3’

MsCib3T131L

5’ TGGGACCTGGAGCAGCTCGTGACCAGGCT 3’ and

5’ AGCTGCTCCAGGTCCCATGCACAGATGTAG 3’

MsCib3L140R

5’ TGACTCGTGGGGAACGGAGTGCTGAGGAA 3’ and

5’ CGTTCCCCACGAGTCAGCCTGGTCACG 3’

MsCib3V148F

5’ GAGGAAGTGACCCTGTTTTGTGAGAAGGTGC 3’ and

5’ AAACAGGGTCACTTCCTCAGCACTCAGTTC 3’

MsCib3V152F

5’ CTGGTCTGTGAGAAGTTTCTGGATGAAGCAG 3’ and

5’ AAACTTCTCACAGACCAGGGTCACTTCCTC 3’

MsTmc1F312R

5’ TTCAGCTGGAAGGTGCGCTGTAGCTGGGAC 3’ and

5’ CGCACCTTCCAGCTGAAGTTGAAAGTGTTGT 3’

MsTmc1W315D

5’ GAAGGTGTTCTGTAGCGACGACTATCTGATTGGT 3’ and

5’ GTCGCTACAGAACACCTTCCAGCTGAAGTTGA 3’

MsTmc1Y317A

5’ TTCTGTAGCTGGGACGCTCTGATTGGTAACCC 3’ and

5’ GCGTCCCAGCTACAGAACACCTTCCAGCT 3’

MsTmc1N321K

5’ GGACTATCTGATTGGTAAACCTGAAACAGCC 3’ and

5’ TTTACCAATCAGATAGTCCCAGCTACAGAACAC 3’

MsTmc1E323K

5’ ATCTGATTGGTAACCCTAAAACAGCCGACAA 3’ and

TAGGGTTACCAATCAGATAGTCCCAGCTAC 3’

MsTmc1N330A

5’ GCCGACAACAAGTTTGCCTCTATCACGATGAA 3’ and

GCAAACTTGTTGTCGGCTGTTTCAGGGTTAC 3’

MsTmc1K337Q

5’ TCTATCACGATGAACTTTCAGGAAGCCATCATA 3’ and

GAAAGTTCATCGTGATAGAGTTAAACTTGTTGTC 3’

MsCib2-E64D

5’ ATCATTCAGATGCCGGACCTCCGGGAGAATC 3’ and

5’ GTCCGGCATCTGAATGATGAGGCTCATGGGT 3’

MsCib2-R66W;

5’ TTCAGATGCCGGAGCTCTGGGAGAATCCCTT 3’ and

5’ AGAGCTCCGGCATCTGAATGATGAGGCTCAT 3’

MsCib2-F91S;

5’ CCTCACCTTCAATGACTCTGTGGACATGTTC 3’ and

5’ GAGTCATTGAAGGTGAGGTTCCCCTCGCCAT 3’

MsCib2-C99W;

5’ ATGTTCTCTGTGCTCTGGGAATCAGCGCCTC 3’ and

5’ CCAGAGCACAGAGAACATGTCCACAAAGTCA 3’

MsCib2-I123T;

5’ CAACACTGACAATTTTACCTGTAAAGAAGAC 3’ and

5’ GTAAAATTGTCAGTGTTGAAGTCATAGATCT 3’

MsCib2-R186W;

5’ AGCACCTTCCACATTTGgATCTCTAGAACTA 3’ and

5’ CCAAATGTGGAAGGTGCTGAGAAAATCAGGG 3’

## QUANTIFICATION AND STATISTICAL ANALYSIS

Data analysis was performed using Excel (Microsoft) and Igor pro 7 (WaveMetrics, Lake Oswego, OR).Transduction current-displacement curves (I(X)) were fitted with the following double Boltzmann (Peng et al., 2013; Peng et al., 2016):

$$I(x) = \frac{I_{max}}{1 + e^{z1(x_0 - x)}\left(1 + e^{Z2(x_0 - x)}\right)}$$

Where $Z_1$ and $Z_2$ are the slope factors and $x_0$ represents the set point.

Current/Voltage plots for reversal potential measurement were fitted with a single-site binding model (Effertz et al., 2017; Farris et al., 2004; Kros et al., 1992). The relative $Ca^{2+}$

permeability, $P_{Ca}/P_{Cs}$, was calculated from the Goldman–Hodgkin–Katz equation (Kim and Fettiplace, 2013, Kim et al., 2013)

Statistical details are described in the Results, Figures and Figure Legends. All data are mean ± SEM. Student's two-tailed unpaired t test was used to determine statistical significance for two group comparisons (*, $p<0.05$, **, $p<0.01$, ***, $p<0.001$). Exact values of n are reported where appropriate. Depending on the experiment, n represents number of animals, number of cells, or number of experiments.

## Supplementary Material

Refer to Web version on PubMed Central for supplementary material.

## Acknowledgements

We thank members of the laboratory for comments and criticisms. We are grateful to C. Hawkins for help generating mouse mutants, and M. Monroe and K. Zhang for assistance with mouse work. Structural work was supported by research conducted at the Northeastern Collaborative Access Team beamlines, which are funded by the National Institute of General Medical Sciences from the National Institutes of Health (P30 GM124165). This research used resources of the Advanced Photon Source, a U.S. Department of Energy (DOE) Office of Science User Facility operated for the DOE Office of Science by Argonne National Laboratory under Contract No. DE-AC02-06CH11357. This work was also supported by the NIH (CLC., F32DC015724; R21DC019195; U.M., RO1DC005965, RO1DC007704, RO1DC014713; L.S. and U.M., RO1DC016960) and the David M. Rubenstein Fund for Hearing Research. U.M. is a Bloomberg Distinguished Professor.

## References

Abecasis GR, Cherny SS, Cookson WO, and Cardon LR (2002). Merlin--rapid analysis of dense genetic maps using sparse gene flow trees. Nat Genet 30, 97–101. [PubMed: 11731797]

Adams PD, Gopal K, Grosse-Kunstleve RW, Hung LW, Ioerger TR, McCoy AJ, Moriarty NW, Pai RK, Read RJ, Romo TD, et al. (2004). Recent developments in the PHENIX software for automated crystallographic structure determination. J Synchrotron Radiat 11, 53–55. [PubMed: 14646133]

An WF, Bowlby MR, Betty M, Cao J, Ling HP, Mendoza G, Hinson JW, Mattsson KI, Strassle BW, Trimmer JS, et al. (2000). Modulation of A-type potassium channels by a family of calcium sensors. Nature 403, 553–556. [PubMed: 10676964]

Assad JA, and Corey DP (1992). An active motor model for adaptation by vertebrate hair cells. J Neurosci 12, 3291–3309. [PubMed: 1527581]

Assad JA, Hacohen N, and Corey DP (1989). Voltage dependence of adaptation and active bundle movement in bullfrog saccular hair cells. Proc Natl Acad Sci U S A 86, 2918–2922. [PubMed: 2468161]

Ballesteros A, Fenollar-Ferrer C, and Swartz KJ (2018). Structural relationship between the putative hair cell mechanotransduction channel TMC1 and TMEM16 proteins. eLife 7.

Berridge MJ, Bootman MD, and Roderick HL (2003). Calcium signalling: dynamics, homeostasis and remodelling. Nature reviews 4, 517–529.

Beurg M, Goldring AC, and Fettiplace R. (2015a). The effects of Tmc1 Beethoven mutation on mechanotransducer channel function in cochlear hair cells. The Journal of general physiology146, 233–243. [PubMed: 26324676]

Beurg M, Kim KX, and Fettiplace R. (2014). Conductance and block of hair-cell mechanotransducer channels in transmembrane channel-like protein mutants. The Journal of general physiology144, 55–69. [PubMed: 24981230]

Beurg M, Xiong W, Zhao B, Muller U, and Fettiplace R. (2015b). Subunit determination of the conductance of hair-cell mechanotransducer channels. Proc Natl Acad Sci U S A112, 1589–1594. [PubMed: 25550511]

Burgoyne RD, Helassa N, McCue HV, and Haynes LP (2019). Calcium Sensors in Neuronal Function and Dysfunction. Cold Spring Harb Perspect Biol 11.

Caprara GA, Mecca AA, and Peng AW (2020). Decades-old model of slow adaptation in sensory hair cells is not supported in mammals. Sci Adv 6, eabb4922. [PubMed: 32851178]

Cheung EL, and Corey DP (2006). Ca2+ changes the force sensitivity of the hair-cell transduction channel. Biophys J 90, 124–139. [PubMed: 16214875]

Choe Y, Magnasco MO, and Hudspeth AJ (1998). A model for amplification of hair-bundle motion by cyclical binding of Ca2+ to mechanoelectrical-transduction channels. Proc Natl Acad Sci U S A 95, 15321–15326. [PubMed: 9860967]

Corns LF, Johnson SL, Kros CJ, and Marcotti W. (2014). Calcium entry into stereocilia drives adaptation of the mechanoelectrical transducer current of mammalian cochlear hair cells. Proc Natl Acad Sci U S A111, 14918–14923. [PubMed: 25228765]

Corns LF, Johnson SL, Kros CJ, and Marcotti W. (2016). Tmc1 Point Mutation Affects Ca2+ Sensitivity and Block by Dihydrostreptomycin of the Mechanoelectrical Transducer Current of Mouse Outer Hair Cells. J Neurosci36, 336–349. [PubMed: 26758827]

Crawford AC, Evans MG, and Fettiplace R. (1989). Activation and adaptation of transducer currents in turtle hair cells. J Physiol419, 405–434. [PubMed: 2621635]

Crawford AC, Evans MG, and Fettiplace R. (1991). The actions of calcium on the mechanoelectrical transducer current of turtle hair cells. J Physiol434, 369–398. [PubMed: 1708822]

Crooks GE, Hon G, Chandonia JM, and Brenner SE (2004). WebLogo: a sequence logo generator. Genome Res 14, 1188–1190. [PubMed: 15173120]

Cunningham CL, and Muller U. (2018). Molecular Structure of the Hair Cell Mechanoelectrical Transduction Complex. Cold Spring Harb Perspect Med.

Cunningham CL, Qiu X, Wu Z, Zhao B, Peng G, Kim YH, Lauer A, and Muller U. (2020). TMIE Defines Pore and Gating Properties of the Mechanotransduction Channel of Mammalian Cochlear Hair Cells. Neuron.

Cunningham CL, Wu Z, Jafari A, Zhao B, Schrode K, Harkins-Perry S, Lauer A, and Muller U. (2017). The murine catecholamine methyltransferase mTOMT is essential for mechanotransduction by cochlear hair cells. eLife6.

Effertz T, Becker L, Peng AW, and Ricci AJ (2017). Phosphoinositol-4,5-Bisphosphate Regulates Auditory Hair-Cell Mechanotransduction-Channel Pore Properties and Fast Adaptation. J Neurosci 37, 11632–11646. [PubMed: 29066559]

Emsley P, and Cowtan K. (2004). Coot: model-building tools for molecular graphics. Acta Crystallogr D Biol Crystallogr60, 2126–2132. [PubMed: 15572765]

Evans PR, and Murshudov GN (2013). How good are my data and what is the resolution? Acta Crystallogr D Biol Crystallogr 69, 1204–1214. [PubMed: 23793146]

Farris HE, LeBlanc CL, Goswami J, and Ricci AJ (2004). Probing the pore of the auditory hair cell mechanotransducer channel in turtle. J Physiol 558, 769–792. [PubMed: 15181168]

Fettiplace R. (2017). Hair Cell Transduction, Tuning, and Synaptic Transmission in the Mammalian Cochlea. Compr Physiol7, 1197–1227. [PubMed: 28915323]

Gentry HR, Singer AU, Betts L, Yang C, Ferrara JD, Sondek J, and Parise LV (2005). Structural and biochemical characterization of CIB1 delineates a new family of EF-hand-containing proteins. J Biol Chem 280, 8407–8415. [PubMed: 15574431]

Giese APJ, Tang YQ, Sinha GP, Bowl MR, Goldring AC, Parker A, Freeman MJ, Brown SDM, Riazuddin S, Fettiplace R, et al. (2017). CIB2 interacts with TMC1 and TMC2 and is essential for mechanotransduction in auditory hair cells. Nat Commun 8, 43. [PubMed: 28663585]

Gillespie PG, and Muller U. (2009). Mechanotransduction by hair cells: models, molecules, and mechanisms. Cell139, 33–44. [PubMed: 19804752]

Goldring AC, Beurg M, and Fettiplace R. (2019). The contribution of TMC1 to adaptation of mechanoelectrical transduction channels in cochlear outer hair cells. J Physiol597, 5949–5961. [PubMed: 31633194]

Holt JR, Gillespie SK, Provance DW, Shah K, Shokat KM, Corey DP, Mercer JA, and Gillespie PG (2002). A chemical-genetic strategy implicates myosin-1c in adaptation by hair cells. Cell 108, 371–381. [PubMed: 11853671]

Howard J, and Hudspeth AJ (1987). Mechanical relaxation of the hair bundle mediates adaptation in mechanoelectrical transduction by the bullfrog's saccular hair cell. Proc Natl Acad Sci U S A 84, 3064–3068. [PubMed: 3495007]

Jia Y, Zhao Y, Kusakizako T, Wang Y, Pan C, Zhang Y, Nureki O, Hattori M, and Yan Z. (2020). TMC1 and TMC2 Proteins Are Pore-Forming Subunits of Mechanosensitive Ion Channels. Neuron105, 310–321e313. [PubMed: 31761710]

Kabsch W. (2010). Biological crystallography. Xds Acta crystallographicaSection D66, 125–132.

Kawashima Y, Geleoc GS, Kurima K, Labay V, Lelli A, Asai Y, Makishima T, Wu DK, Della Santina CC, Holt JR, et al. (2011). Mechanotransduction in mouse inner ear hair cells requires transmembrane channel-like genes. J Clin Invest 121, 4796–4809. [PubMed: 22105175]

Kennedy HJ, Evans MG, Crawford AC, and Fettiplace R. (2003). Fast adaptation of mechanoelectrical transducer channels in mammalian cochlear hair cells. Nat Neurosci6, 832–836. [PubMed: 12872124]

Kim KX, Beurg M, Hackney CM, Furness DN, Mahendrasingam S, and Fettiplace R. (2013). The role of transmembrane channel-like proteins in the operation of hair cell mechanotransducer channels. The Journal of general physiology142, 493–505. [PubMed: 24127526]

Kim KX, and Fettiplace R. (2013). Developmental changes in the cochlear hair cell mechanotransducer channel and their regulation by transmembrane channel-like proteins. The Journal of general physiology141, 141–148. [PubMed: 23277480]

Kros CJ, Rusch A, and Richardson GP (1992). Mechano-electrical transducer currents in hair cells of the cultured neonatal mouse cochlea. Proc Biol Sci 249, 185–193. [PubMed: 1280836]

Kurima K, Ebrahim S, Pan B, Sedlacek M, Sengupta P, Millis BA, Cui R, Nakanishi H, Fujikawa T, Kawashima Y, et al. (2015). TMC1 and TMC2 Localize at the Site of Mechanotransduction in Mammalian Inner Ear Hair Cell Stereocilia. Cell reports 12, 1606–1617. [PubMed: 26321635]

Kurima K, Peters LM, Yang Y, Riazuddin S, Ahmed ZM, Naz S, Arnaud D, Drury S, Mo J, Makishima T, et al. (2002). Dominant and recessive deafness caused by mutations of a novel gene, TMC1, required for cochlear hair-cell function. Nat Genet 30, 277–284. [PubMed: 11850618]

Labay V, Weichert RM, Makishima T, and Griffith AJ (2010). Topology of transmembrane channel-like gene 1 protein. Biochemistry 49, 8592–8598. [PubMed: 20672865]

Landau M, Mayrose I, Rosenberg Y, Glaser F, Martz E, Pupko T, and Ben-Tal N. (2005). ConSurf 2005: the projection of evolutionary conservation scores of residues on protein structures. Nucleic Acids Res33, W299–302. [PubMed: 15980475]

Maoileidigh D, and Ricci AJ (2019). A Bundle of Mechanisms: Inner-Ear Hair-Cell Mechanotransduction. Trends Neurosci 42, 221–236. [PubMed: 30661717]

Michel V, Booth KT, Patni P, Cortese M, Azaiez H, Bahloul A, Kahrizi K, Labbe M, Emptoz A, Lelli A, et al. (2017). CIB2, defective in isolated deafness, is key for auditory hair cell mechanotransduction and survival. EMBO Mol Med 9, 1711–1731. [PubMed: 29084757]

Pan B, Akyuz N, Liu XP, Asai Y, Nist-Lund C, Kurima K, Derfler BH, Gyorgy B, Limapichat W, Walujkar S, et al. (2018). TMC1 Forms the Pore of Mechanosensory Transduction Channels in Vertebrate Inner Ear Hair Cells. Neuron 99, 736–753 e736. [PubMed: 30138589]

Pan B, Geleoc GS, Asai Y, Horwitz GC, Kurima K, Ishikawa K, Kawashima Y, Griffith AJ, and Holt JR (2013). TMC1 and TMC2 are components of the mechanotransduction channel in hair cells of the mammalian inner ear. Neuron 79, 504–515. [PubMed: 23871232]

Patel K, Giese AP, Grossheim JM, Hegde RS, Delio M, Samanich J, Riazuddin S, Frolenkov GI, Cai J, Ahmed ZM, et al. (2015). A Novel C-Terminal CIB2 (Calcium and Integrin Binding Protein 2) Mutation Associated with Non-Syndromic Hearing Loss in a Hispanic Family. PLoS One 10, e0133082. [PubMed: 26426422]

Peng AW, Effertz T, and Ricci AJ (2013). Adaptation of mammalian auditory hair cell mechanotransduction is independent of calcium entry. Neuron 80, 960–972. [PubMed: 24267652]

Peng AW, Gnanasambandam R, Sachs F, and Ricci AJ (2016). Adaptation Independent Modulation of Auditory Hair Cell Mechanotransduction Channel Open Probability Implicates a Role for the Lipid Bilayer. J Neurosci 36, 2945–2956. [PubMed: 26961949]

Pioletti M, Findeisen F, Hura GL, and Minor DL Jr. (2006). Three-dimensional structure of the KChIP1-Kv4.3 T1 complex reveals a cross-shaped octamer. Nat Struct Mol Biol 13, 987–995. [PubMed: 17057713]

Riazuddin S, Belyantseva IA, Giese AP, Lee K, Indzhykulian AA, Nandamuri SP, Yousaf R, Sinha GP, Lee S, Terrell D, et al. (2012). Alterations of the CIB2 calcium- and integrin-binding protein cause Usher syndrome type 1J and nonsyndromic deafness DFNB48. Nat Genet 44, 1265–1271. [PubMed: 23023331]

Ricci AJ, and Fettiplace R. (1997). The effects of calcium buffering and cyclic AMP on mechano-electrical transduction in turtle auditory hair cells. J Physiol501 (Pt 1), 111–124. [PubMed: 9174998]

Romani AM, and Scarpa A. (2000). Regulation of cellular magnesium. Front Biosci5, D720–734. [PubMed: 10922296]

Roy A, Kucukural A, and Zhang Y. (2010). I-TASSER: a unified platform for automated protein structure and function prediction. Nature protocols, 5(4), 725–738. [PubMed: 20360767]

Scannevin RH, Wang K, Jow F, Megules J, Kopsco DC, Edris W, Carroll KC, Lu Q, Xu W, Xu Z, et al. (2004). Two N-terminal domains of Kv4 K(+) channels regulate binding to and modulation by KChIP1. Neuron 41, 587–598. [PubMed: 14980207]

Seco CZ, Giese AP, Shafique S, Schraders M, Oonk AM, Grossheim M, Oostrik J, Strom T, Hegde R, van Wijk E, et al. (2016). Novel and recurrent CIB2 variants, associated with nonsyndromic deafness, do not affect calcium buffering and localization in hair cells. Eur J Hum Genet 24, 542–549. [PubMed: 26173970]

Tang YQ, Lee SA, Rahman M, Vanapalli SA, Lu H, and Schafer WR (2020). Ankyrin Is An Intracellular Tether for TMC Mechanotransduction Channels. Neuron.

Vallone R, Dal Cortivo G, D'Onofrio M, and Dell'Orco D. (2018). Preferential Binding of Mg(2+) Over Ca(2+) to CIB2 Triggers an Allosteric Switch Impaired in Usher Syndrome Type 1J. Front Mol Neurosci11, 274. [PubMed: 30174586]

Wang H, Yan Y, Liu Q, Huang Y, Shen Y, Chen L, Chen Y, Yang Q, Hao Q, Wang K, et al. (2007). Structural basis for modulation of Kv4 K+ channels by auxiliary KChIP subunits. Nat Neurosci 10, 32–39. [PubMed: 17187064]

Wang K. (2008). Modulation by clamping: Kv4 and KChIP interactions. Neurochem Res33, 1964–1969. [PubMed: 18415675]

Wang Y, Li J, Yao X, Li W, Du H, Tang M, Xiong W, Chai R, and Xu Z. (2017). Loss of CIB2 Causes Profound Hearing Loss and Abolishes Mechanoelectrical Transduction in Mice. Front Mol Neurosci10, 401. [PubMed: 29255404]

Xiong W, Grillet N, Elledge HM, Wagner FJ, Zhao B, Johnson KR, Kazmierczak P, and Müller U. (2012). TMHS is an integral component of the mechanotransduction machinery of cochlear hair cells. Cell151.

Xiong W, Wagner T, Yan L, Grillet N, and Muller U. (2014). Using injectoporation to deliver genes to mechanosensory hair cells. Nature protocols9, 2438–2449. [PubMed: 25232939]

Zhao B, Wu Z, Grillet N, Yan L, Xiong W, Harkins-Perry S, and Muller U. (2014). TMIE Is an Essential Component of the Mechanotransduction Machinery of Cochlear Hair Cells. Neuron84, 954–967. [PubMed: 25467981]

Zhao B, Wu Z, and Muller U. (2016). Murine Fam65b forms ring-like structures at the base of stereocilia critical for mechanosensory hair cell function. eLife5.

Zhou W, Qian Y, Kunjilwar K, Pfaffinger PJ, and Choe S. (2004). Structural insights into the functional interaction of KChIP1 with Shal-type K(+) channels. Neuron41, 573–586. [PubMed: 14980206]

## Highlights

- CIB2 and CIB3 resemble KChIP proteins
- Co-crystals show that a hydrophobic groove in CIB2/3 mediates TMC1/2 binding
- CIB2 regulates the transport of TMC1 and TMC2 into stereocilia
- CIB2 point mutations affect MET channel function.

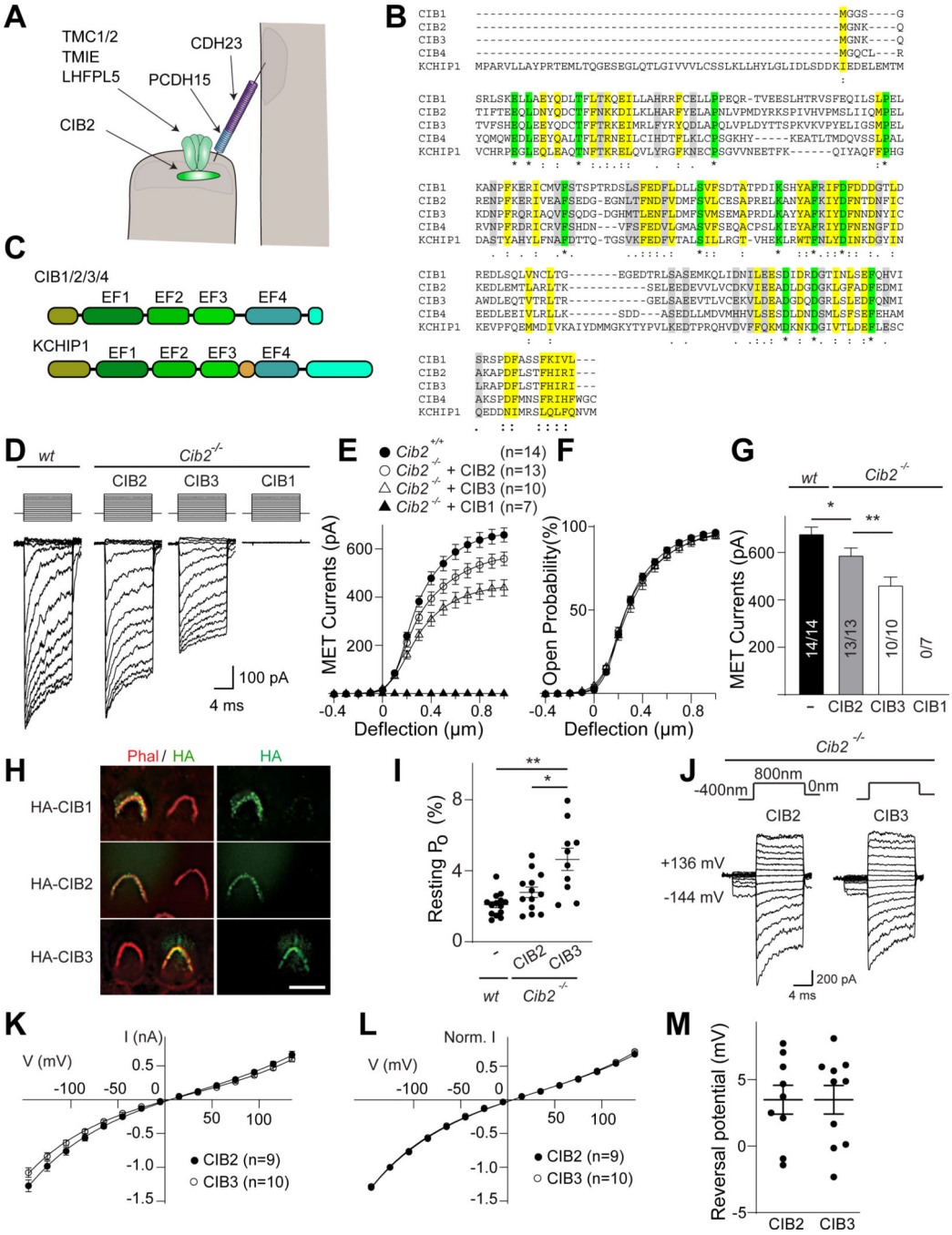


**Figure 1. CIB2 and CIB3 are functionally interchangeable.**

(A) Diagram of the MET complex. (B) Sequence alignment of mouse CIB1–4 and KChIP1 using Clustal Omega (green: fully conserved amino acids; yellow: conservation between amino acids with similar properties; grey: conservation between amino acids of weakly similar properties). (C) Diagram of CIB1–4 and KChIP1. (D) Representative MET currents in OHCs from wild-type (*wt*) and *Cib2*$^{-/-}$ mice at P3 + 2 day in vitro (DIV) after injectoporation of the indicated constructs. Currents are in response to 10 ms hair bundle deflections from −400 nm to 1000 nm. (E) Current/displacement (I/X) plots from data as

in (D) (n = number of cells; mean ± SEM). (F) Open probability/displacement plots from similar data as in (D) (n = number of cells; mean ± SEM). (G) Peak currents obtained from double Gaussian fitting of I/X plots in E (n = number of cells which can evoke MET currents in total recorded cells; mean ± SEM; * $p<0.05$, ** $p<0.01$). (H) Examples of P3 + 1 DIV OHCs from *Cib2*$^{-/-}$ mice injectoporated with the indicated constructs and immunostained for HA (green) and phalloidin (red). (I) Channel open probability at rest obtained from (F) at zero deflection (mean ± SEM; * $p<0.05$, ** $p<0.01$). (J) Reversal potential: hair cell was held at various potentials (20 mV increments from −144 mV to +136 mV); hair bundles were mechanically stimulated to elicit currents. Top, mechanical stimulus paradigm; bottom, representative MET currents in OHCs from *Cib2*$^{-/-}$ cells injectoporated to express CIB2 or CIB3. (K). Current/voltage plots averaged at various membrane potentials for data as in (J). (L) Current/voltage relations were normalized to currents at −124mV to account for differences in current amplitude in controls and mutants. Current/voltage plots were fitted with a single-site binding model. (M) Reversal potential ($R_V$) plots for OHCs calculated from (K,L). Scale bar, 5 μm. See also Fig. S1.

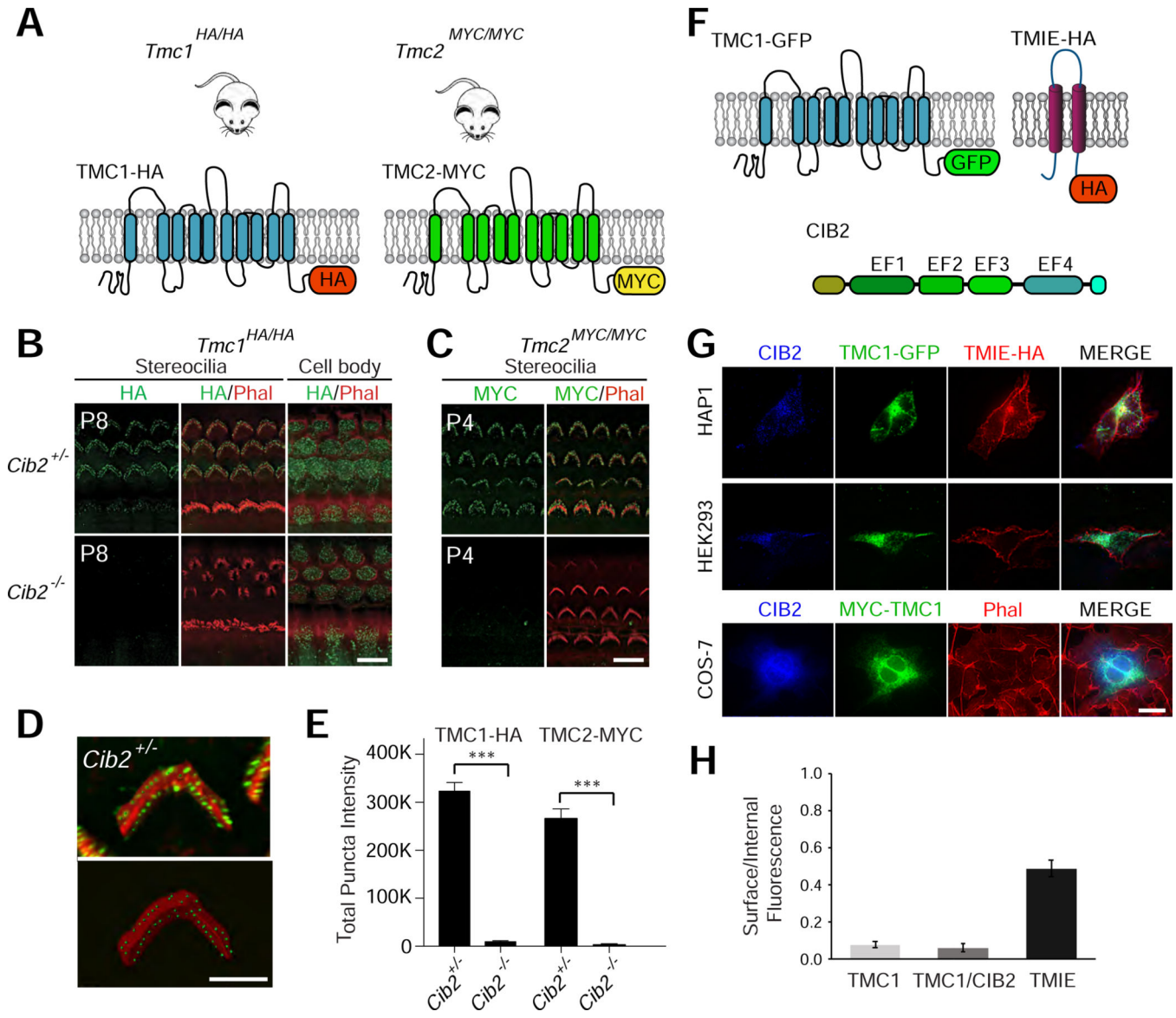


**Figure 2. CIB2 affects TMC1 and TMC2 localization to stereocilia.**

(A) Diagram of the *Tmc1*$^{HA}$ and *Tmc2*$^{MYC}$ mouse lines. (B,C) Cochlear whole mounts from mice of the indicated genetic background and age were stained with phalloidin (red) and antibodies to HA and MYC (green) to detect TMC1-HA (B) and TMC2-MYC (C). (D) Representative Imaris 9.1 image used for quantification. (E) Quantification of expression levels of TMC1-HA and TMC2-MYC in hair bundles was accomplished by summing the mean intensity of all HA- or MYC-positive puncta located within each phalloidin-positive bundle from OHCs (n=6 for each genotype; mean ± SEM; *** $p<0.001$. (F) Diagram of proteins expressed by transfection in cell lines. (G) Immunofluorescence images of the indicated cell lines transfected to co-express CIB2, TMIE-HA and TMC1-GFP. For COS-7 cells, phalloidin staining (PHAL) is shown. The three rows show three representative cells. (H) Quantification of surface/internal fluorescence for TMC1 or TMIE for combinations of constructs transfected in COS-7 cells (n=11 for TMC1 only; n=15 for TMC1/CIB2 and

n=10 for TMIE). Scale bar in C: 10 μm, applies to B-C. Scale bar in D: 5 μm, Scale bar in G: 10 μm.

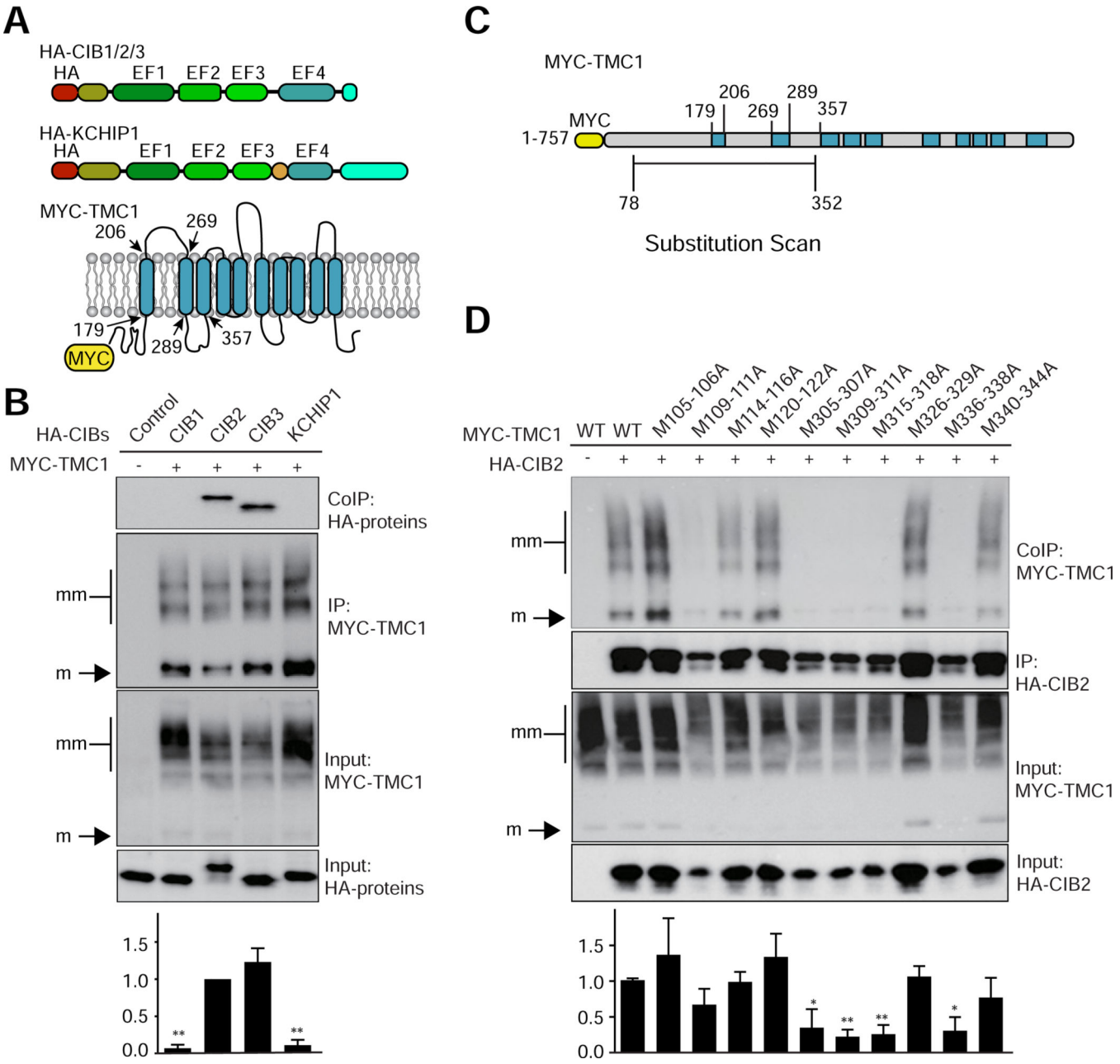


**Figure 3. Mapping of the CIB2 binding site in TMC1.**

(A) Diagram of constructs used for co-immunoprecipitation experiments. (B) HEK293 cells were transfected with the constructs indicated on top of each panel. Immunoprecipitations (IP) were carried out with MYC-conjugated agarose beads, followed by western blotting to detect epitope-tagged proteins (upper rows, CoIP; middle rows, IP; lower rows, input). MYC-TMC1 multimers (mm) and monomers (m) are indicated). Quantification of CoIP results from at least 3 independent experiments are below. Binding of constructs to MYC-TMC1 was normalized to CIB2 values (mean ± SEM; **, $p<0.01$). (C) Diagrams of MYC-TMC1 amino acid substitution constructs. (D) HEK293 cells were transfected with the constructs indicated on top of each panel. Labels on top indicated amino acids (M) changed

to Ala (A). Immunoprecipitations (IP) were carried out with HA-conjugated agarose beads, followed by western blotting with antibodies to the MYC-tag to detect epitope-tagged TMC1 proteins. Quantification (below) of CoIP results (≥ 3 experiments) normalized to MYC-TMC1 wild-type (WT) values (mean ± SEM; *, $p<0.05$; **, $p<0.01$; ***, $p<0.001$). See also Fig. S2 and S3.

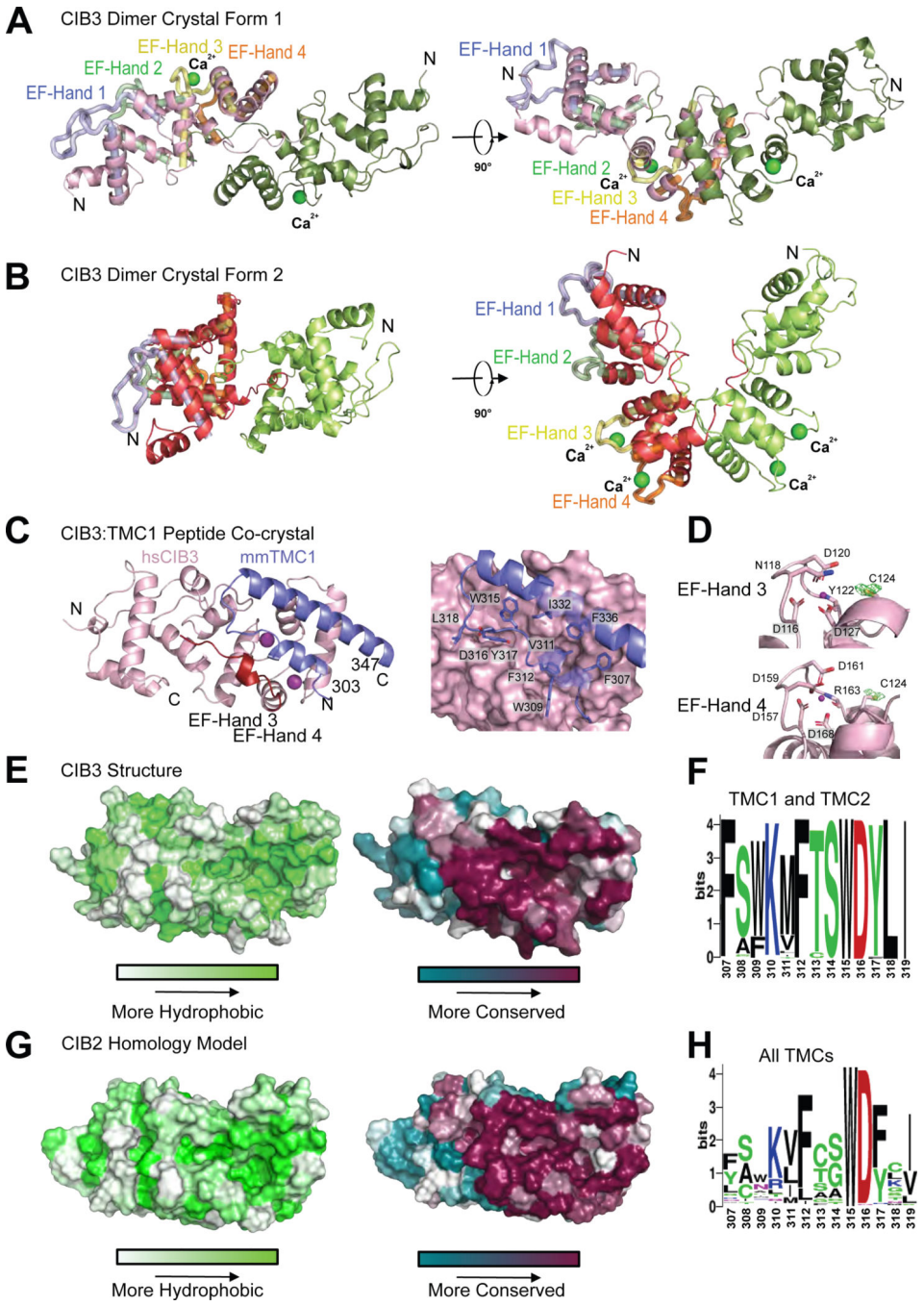


**Figure 4. Structure of CIB3 homodimer in two crystal forms.**

(A and B) Dimers of CIB3 from two crystal forms shown in orthogonal views. Different protomers are represented by shades of pink and green, $Ca^{2+}$ as green spheres. (C) Crystal structure of the CIB3:TMC1 complex with CIB3 shown in pink and TMC1 peptide in slate. The C-terminal domain of CIB3 that swaps in the homodimer is colored red. $Mg^{2+}$ represented as purple spheres. (D) Left: Close up view of TMC1 (ribbon) in complex with CIB3 (surface) with the side chains of key residues shown in stick representation and labeled. The N-terminal alpha helix has been made transparent to aid in visualization

of Phe312. Right: Bijvoet difference map density, in green mesh, shows a lack of $Ca^{2+}$ occupancy in EF-hands 3 and 4. Ligand side chains are labeled and represented in sticks. $Mg^{2+}$ ions are represented as small purple spheres. Anomalous density for the sulfur atom of Cys124 is shown. (E) Left: Surface representation of CIB3 colored according to Eisenberg hydrophobicity scale. Right: View of the TMC1-peptide binding site with conservation scores from ConSurf mapped onto the structure. Color key is provided, with low conservation being teal and high conservation in burgundy (Landau et al., 2005). (F) Sequence logo for the TMC1 binding domain, generated from sequence alignments of TMC1 and TMC2. Numbering corresponds to full-length mouse sequence (Crooks et al., 2004). (G) Left: Surface representation of CIB2 homology model colored according to the Eisenberg hydrophobicity scale. Right: Conservation scores as in panel (E). (H) Sequence logo for the TMC1 binding domain, generated from sequence alignment across the TMC family. Numbering corresponds to full length mouse sequence (Crooks et al., 2004). See also Fig. S4, Fig. S5 and Table S1.

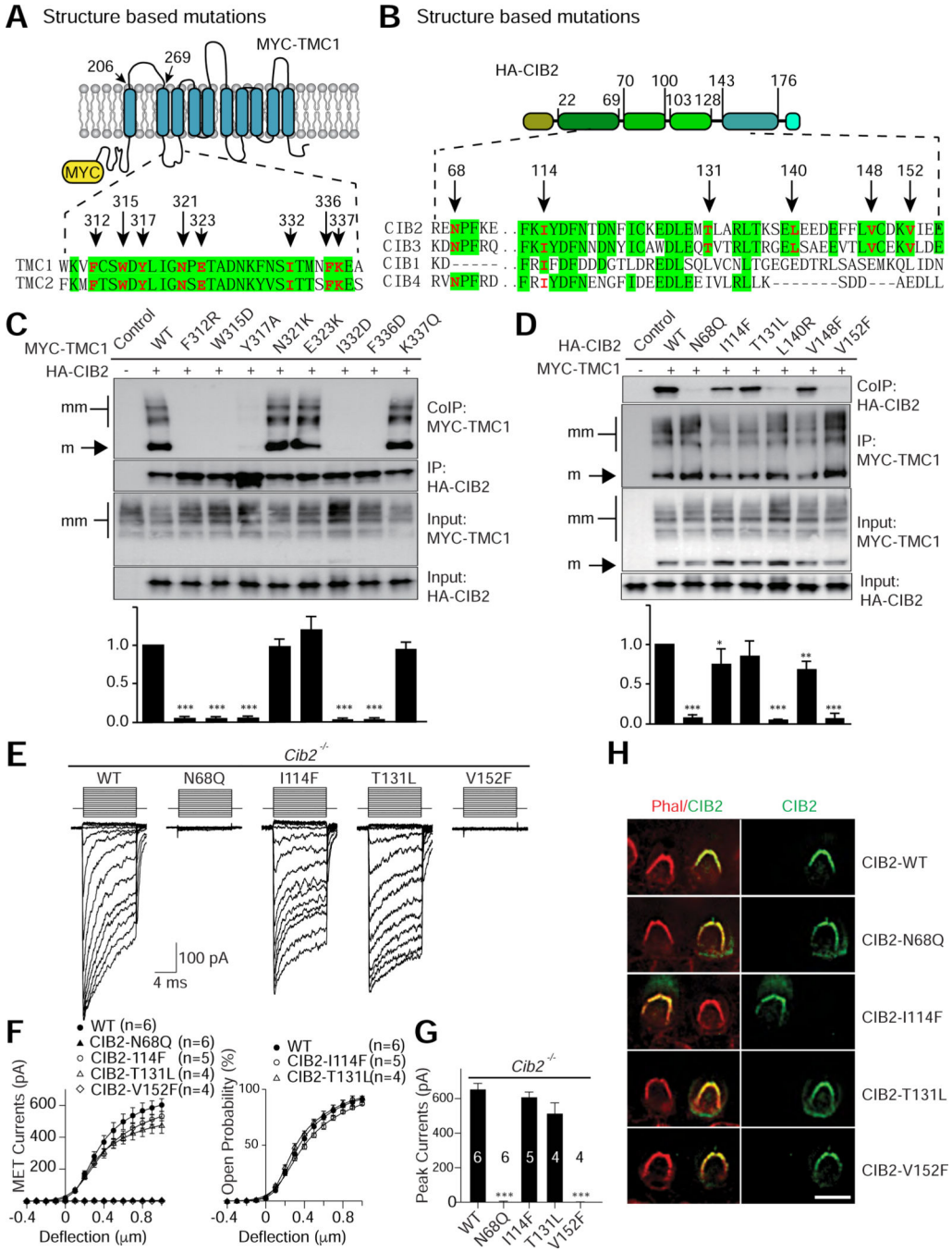


**Figure 5. Mutational analysis of amino acids mediating contact between TMC1 and CIB2.**

(A,B) Diagram of MYC-TMC1 (A) and HA-CIB2 (B) indicating in red the position of mutagenized amino acids. Amino acids conserved between TMC1 and TMC2 and between CIB1–4 highlighted in green. (C,D) HEK293 cells were transfected with the constructs indicated on top of each panel. Immunoprecipitations were carried out with HA- or MYC-conjugated agarose beads, followed by western blotting with antibodies to the MYC- or HA-tag to detect epitope-tagged TMC and CIB2 proteins, respectively. Quantification below of CoIP results from ≥3 experiments normalized to MYC-TMC1 or HA-CIB2 wild-type

(WT) values (mean ± SEM; *, p<0.05; **, p<0.01; ***, p<0.001). Abbreviations as in Fig. 3. (E) Representative MET currents in OHCs from *Cib2*$^{-/-}$ mice at P3 + 2 day in vitro (DIV) after injectoporation of the indicated constructs. Currents are in response to 10 ms hair bundle deflections from −400 nm to 1000 nm. (F) Current/displacement and open probability/displacement plots from data as in (E) (n = number of cells; mean ± SEM). (G) Peak currents obtained from double Gaussian fitting of I/X plots in E (n = number of cells; mean ± SEM; ***, p<0.001). (H) Examples of OHCs from P3+1 DIV *Cib2*$^{-/-}$ mice injectoporated with the indicated constructs and immunostained for CIB2 (green) and phalloidin (red). Scale bar in H: 5 μm. See also Fig. S6.

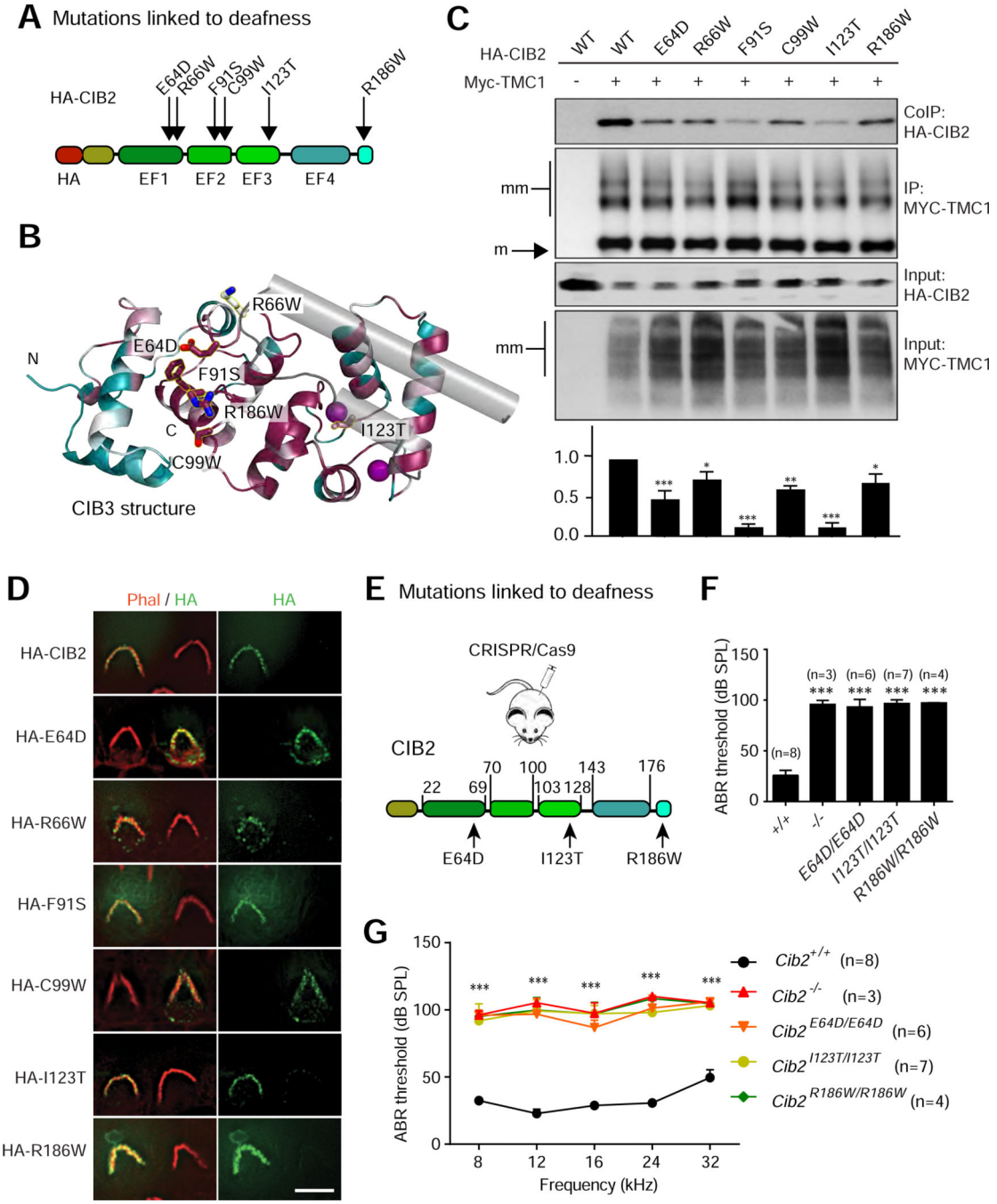


**Figure 6. Analysis of CIB2 proteins carrying mutations linked to deafness.**

(A) Diagram of CIB2 indicating deafness-associated mutations. (B) Mutations indicated on the CIB3 structure. TMC1 peptide shown in grey. (C) HEK293 cells were transfected with the constructs indicated on top of each panel. Immunoprecipitations were carried out with MYC-conjugated agarose beads, followed by western blotting with HA antibodies to detect epitope-tagged CIB2 proteins. Abbreviations as in Fig. 3. Quantification below of CoIP results from ≥3 experiments normalized to HA-CIB2 wild-type (WT) values (mean ± SEM; *, p<0.05; **, p<0.01; ***, p<0.001). (D) OHCs from *Cib2*$^{-/-}$ mice at P3 + 1

DIV injectoporated with the indicated constructs and immunostained for HA (green) and phalloidin (red). (E) Diagram depicting CIB2 point mutations introduced into mice using CRISPR/Cas9. (F,G) Auditory brainstem response (ABR) thresholds in response to click (F) and pure tone (G) stimuli for the indicated mutant mouse lines at 4–6 weeks of age (n = number of mice; mean ± SEM; ***, $p<0.001$). Scale bar in D: 5 μm. See also Fig. S7.

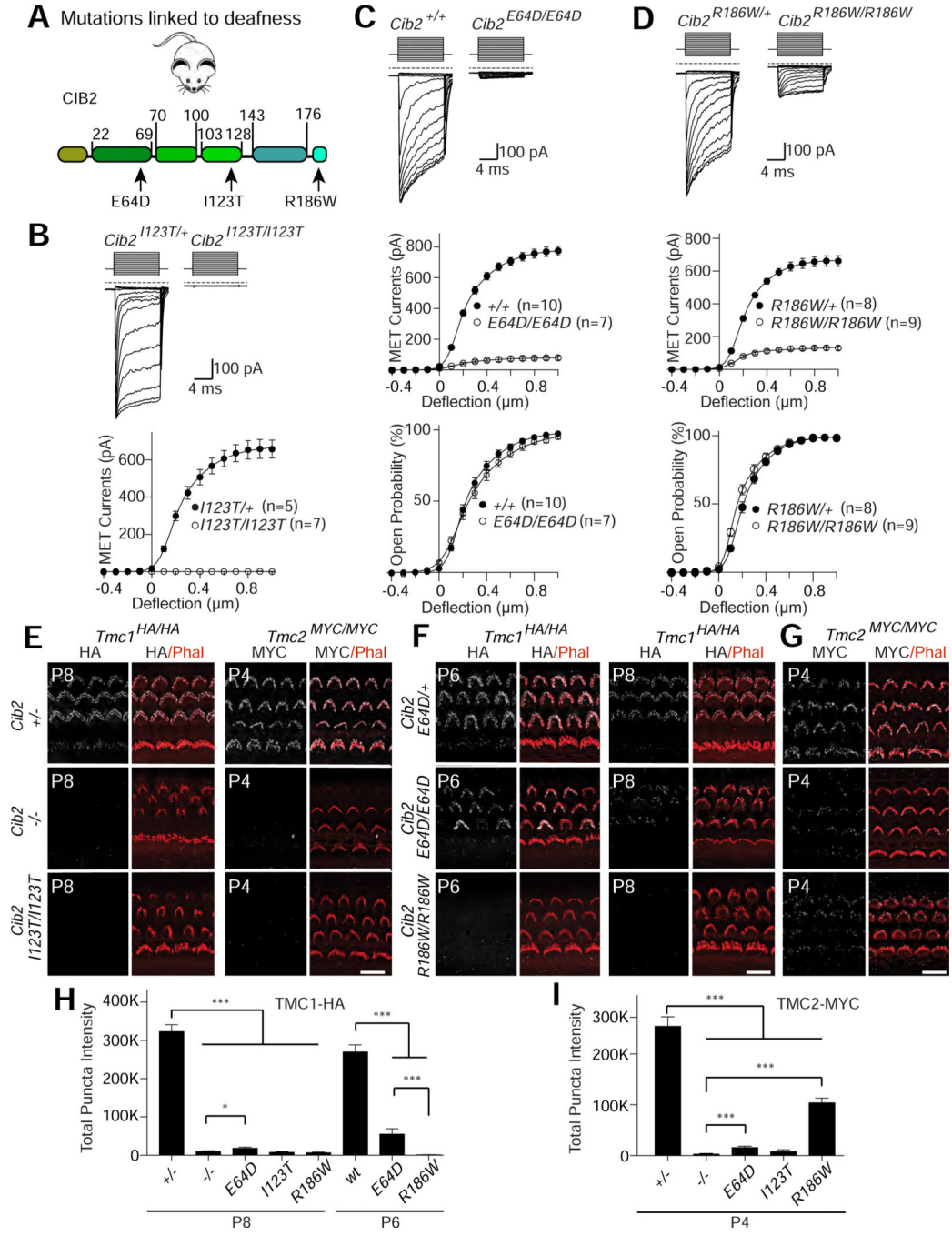


**Figure 7. Analysis of CIB2 mutations linked to deafness.**

(A) Diagram of the mutant mouse lines analyzed. (B-D) Top: Representative MET currents in OHCs from control mice and the indicated mutant mouse lines at P5–6 in response to a set of 10 ms hair bundle deflections ranging from −400 nm to 1000 nm (100 nm steps) using a stiff probe. Bottom (B) and middle (C,D): current/displacement plots (mean ± SEM). Bottom (C,D): open probability/displacement plots (mean ± SEM). (E-G) Cochlear whole mounts from mice of the indicated genetic background and age were stained with phalloidin (red) and antibodies to HA and MYC (white) to detect TMC1-HA (E,F) and TMC2-MYC

(E,G). (H,I) Quantification of expression levels of TMC1-HA (H) and TMC2-MYC (I) in hair bundles was accomplished by summing the mean intensity of all HA- or MYC-positive puncta located within each phalloidin-positive bundle from OHCs (n=6 for each genotype; mean ± SEM; * $p<0.05$, *** $p<0.001$). Note that images from *Cib2*$^{+/-}$ and Cib2$^{-/-}$ are as in Fig. 2. Scale bars: (E-G) 10 μm. See also Fig. S7.

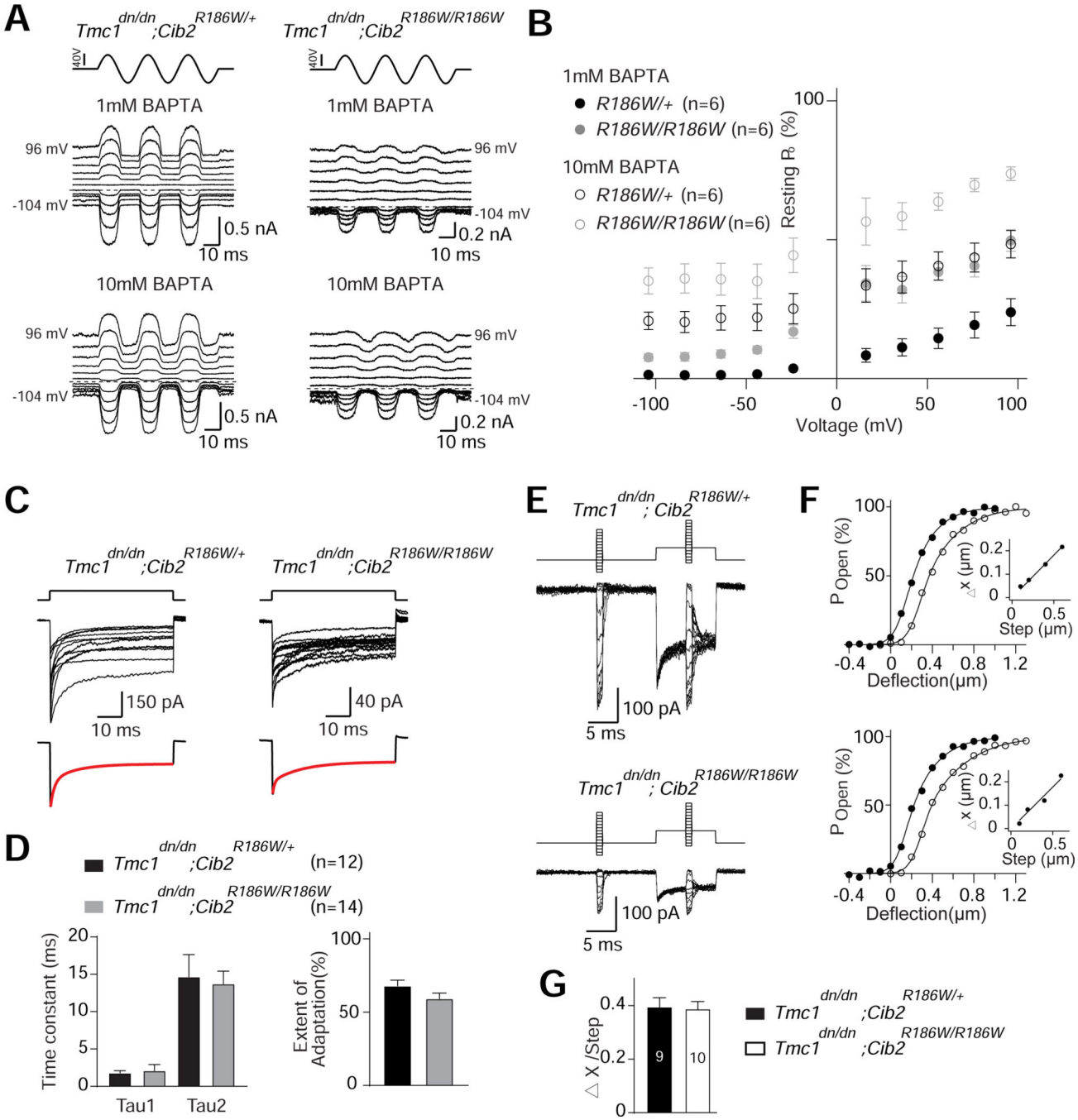


**Figure 8. Analysis of MET channel properties.**

(A) Representative MET currents evoked with sinusoidal fluid deflection of hair bundles from OHCs of *Tmc1*$^{dn/dn}$;*Cib2*$^{R186W/+}$ and *Tmc1*$^{dn/dn}$;*Cib2*$^{R186W/R186W}$ mice at membrane holding potential from −104mV to +96mV. Intracellular $Ca^{2+}$ buffer indicated on top of each panel. (B) Resting $P_o$ / voltage plots obtained from averaged data as in (A). Mouse line and $Ca^{2+}$ buffer indicated left in the panel (n = number of cells; mean ± SEM). (C) Top: Deflection evoked MET currents (50ms, 400nm) recorded from OHCs of *Tmc1*$^{dn/dn}$;*Cib2*$^{R186W/+}$ and *Tmc1*$^{dn/dn}$;*Cib2*$^{R186W/R186W}$ mice as indicated. The adaptation

process of each trace was fitted with a double exponential equation and yielded fast (tau1) and slow (tau2) time constants. Bottom: Averaged MET currents (black) and fitted with double exponential equation (red). (D) Left: fast and slow time constant plots for adaptation obtained from data in (C); Right: extent of adaptation calculated as the ratio of reduced current at steady state to the peak current from data in (C). (E) Representative MET currents in response to a paired-pulse stimulus protocol (400nm steps) as indicated. (F), Current-displacement plots of traces in F fitted with double Boltzmann equation (dots: first stimulus; circle: second stimulus). Inset shows the change in $X_0(\Delta X)$/ pre-displacement plot from the same cell; the adaptive shift was calculated from the slope of linear fitting. (G) Summary plots of adaptive shifts obtained from similar data in E-F (mean ± SEM). See also Fig. S8.

## KEY RESOURCES TABLE

| REAGENT or RESOURCE | SOURCE | IDENTIFIER |
|---|---|---|
| Antibodies | | |
| Rabbit anti-HA | Cell Signaling | Cat#: 3724; RRID:AB_1549585 |
| Rabbit anti-MYC | Cell Signaling | Cat#: 2278; RRID:AB_490778 |
| Rabbit anti-CIB2 | This Paper | N/A |
| Mouse anti-HA | Cell Signaling | Cat#: 2367S; RRID: AB_10691311 |
| Mouse anti-MYC | Cell Signaling | Cat#: 2276S; RRID: AB_331783 |
| Goat anti-Rabbit IgG F(ab')2, Alexa Fluor 488 | Invitrogen | Cat#: A-11070; RRID:AB_2534114 |
| Goat anti-Rabbit IgG F(ab')2, Alexa Fluor 555 | Invitrogen | Cat#: A-21430; RRID:AB_2535851 |
| Goat anti-Mouse IgG F(ab')2, Alexa Fluor 647 | Invitrogen | Cat#: A-21237; RRID:AB_2535806 |
| EZ-View Red HA Affinity Gel | Sigma | Cat#: E6779-1ML; RRID:AB_10109562 |
| EZ View Red anti-c-MYC Affinity Gel | Sigma | Cat#: E6654-1ML; RRID:AB_10093201 |
| Veriblot | Abcam | Cat#: ab131366 |
| Veriblot anti-Mouse | Abcam | Cat#: ab131368 |
| Chemicals, Peptides, and Recombinant Proteins | | |
| Cas9 Protein | PNA Bio | Cat#: CP01-20 |
| Tris-HCl | Sigma | Cat#: T5941 |
| EDTA | Sigma | Cat#: E5134 |
| DMEM+Glutamax medium | Gibco | Cat#: 10569-010 |
| Antibiotic-Antimycotic supplement | Gibco | Cat#: 15240-062 |
| DMEM/F12 medium | Gibco | Cat#: 11330-032 |
| Fetal Bovine Serum, Heat Inactivated | Sigma | Cat#: F4135 |
| Ampicillin | Sigma | Cat#: A9518 |
| Sodium Chloride | VWR | Cat#: 0241 |
| Sodium phosphate monobasic | Sigma | Cat#: S8282 |
| Potassium Chloride | Fisher Scientific | Cat#: P217 |
| Calcium Chloride | Fisher Scientific | Cat#: M13841 |
| Magnesium Chloride | Sigma | Cat#: M8266 |
| Glucose | Sigma | Cat#: G7021 |
| HEPES | Sigma | Cat#: H4034 |
| BAPTA | Sigma | Cat#: A4926 |
| EGTA | VWR | Cat#: 0732 |
| Magnesium-ATP | Sigma | Cat#: A9187 |
| Sodium-GTP | Sigma | Cat#: G8877 |
| Cesium Chloride | Sigma | Cat#: 203025 |
| DMSO | Sigma | Cat#: D2650 |
| Paraformaldehyde | Electron Microscopy Sciences | Cat#: 15714 |
| 1X HBSS medium | Gibco | Cat#: 14175095 |

| REAGENT or RESOURCE | SOURCE | IDENTIFIER |
|---|---|---|
| Normal Goat Serum, Heat Inactivated | Gemini Biosciences | Cat#: 100-109 |
| Triton X-100 | Sigma | Cat#: T9284 |
| Alexa Fluor 555 Phalloidin | Life Technologies | Cat#: A34055 |
| Prolong Gold | ThermoFisher | Cat#: P10144 |
| Lipofectamine 3000 | ThermoFisher | Cat#: L3000015 |
| Tris/Tham | Fisher | Cat#: T370-3 |
| NP-40 | Sigma | Cat#: I3021 |
| Sodium Deoxycholate | Sigma | Cat#: 6750 |
| Sodium Dodecyl Sulfate | Sigma | Cat#: 75746 |
| Complete Mini Protease Inhibitor Tablet, EDTA-free | Roche | Cat#: 11836170001 |
| 4x Laemmli Sample Buffer | Biorad | Cat#: 1610747 |
| 2-Mercaptoethanol | Biorad | Cat#: 1610710 |
| Novex™ WedgeWell™ 4 to 20%, Tris-Glycine, 1.0 mm, Mini Protein Gel | Life Technologies | Cat#: XP04202BOX |
| 10x Tris/Glycine/SDS | Biorad | Cat#: 1610732 |
| 10x Tris/Glycine Buffer for Western Blots and Native Gels | Biorad | Cat#: 1610734 |
| Methanol | VWR | Cat#: BDH1135-4LP |
| ECL Prime Blocking Reagent | GE | Cat#: RPN418 |
| Tween-20 | Sigma | Cat#: P7949 |
| Clarity Western ECL Substrate | Bio-Rad | Cat#: 1705060 |
| Bovine Serum Albumin, fatty acid free | Sigma | Cat#: A8806 |
| Deposited Data | | |
| hsCIB3 | This Paper | PDB: 6WU5 |
| hsCIB3 EK150151QH | This Paper | PDB: 6WU7 |
| hsCIB3:msTmc1 | This Paper | PDB: 6WUD |
| Experimental Models: Cell Lines | | |
| Human: HEK-293 | ATCC | Cat#: CRL-1573 |
| Human: HAP-1 | Horizon | Cat#: C631 |
| Monkey: COS-7 | ATCC | Cat#: CRL-1651 |
| Experimental Models: Organisms/Strains | | |
| *Cib2*$^{Tm1a}$ mice | EUCOMM | N/A |
| *Cib2-E64D* mice | This paper | N/A |
| *Cib2-I123T* mice | This paper | N/A |
| *Cib2-R186W* mice | This paper | N/A |
| *C57BL/6J* mice | Jackson Laboratories | Cat#: 000664; RRID:IMSR JAX:000664 |
| *ICR* mice | Envigo | Cat#: Hsd:ICR (CD-1) |
| Oligonucleotides | | |
| Target-specific crRNAs | This paper/IDT | N/A |
| tracrRNA | Dharmacon | Cat#: U-002005-05 |

| REAGENT or RESOURCE | SOURCE | IDENTIFIER |
|---|---|---|
| Target-specific ssDNA | This paper/IDT Ultramer DNA Oligos | N/A |
| Recombinant DNA | | |
| pN3 | Zhao et al 2014 | N/A |
| pN3-MYC-msTmc1 | Zhao et al 2014 | N/A |
| pN3-MYC-msTmc2 | Zhao et al 2014 | N/A |
| pN3-msTMIE-HA | Zhao et al 2014 | N/A |
| pN3-HA-msCib1 | This paper | N/A |
| pN3-HA-msCib2 | This paper | N/A |
| pN3-HA-msCib3 | This paper | N/A |
| pN3-HA-msKChIP1 | This paper | N/A |
| pN3-HA-msCib2-E64D | This paper | N/A |
| pN3-HA-msCib2-R66W | This paper | N/A |
| pN3-HA-msCib2-F91S | This paper | N/A |
| pN3-HA-msCib2-C99W | This paper | N/A |
| pN3-HA-msCib2-I123T | This paper | N/A |
| pRK5-HA-msCib2-N68Q | This paper | N/A |
| pRK5-HA-msCib2-I114F | This paper | N/A |
| pRK5-HA-msCib2-T131L | This paper | N/A |
| pRK5-HA-msCib2-L140R | This paper | N/A |
| pRK5-HA-msCib2-V148R | This paper | N/A |
| pRK5-HA-msCib2-V152R | This paper | N/A |
| pRK5-HA-msCib3-N68Q | This paper | N/A |
| pRK5-HA-msCib3-I114F | This paper | N/A |
| pRK5-HA-msCib3-T131L | This paper | N/A |
| pRK5-HA-msCib3-L140R | This paper | N/A |
| pRK5-HA-msCib3-V148R | This paper | N/A |
| pRK5-HA-msCib3-V152R | This paper | N/A |
| pCAGEN | Matsuda et al 2004 | Cat#: Addgene #11160; RRID:Addgene_11160 |
| pCAGEN-msTMC1-GFP | This paper | N/A |
| pCAGEN-msCib1-IRES-GFP | This paper | N/A |
| pCAGEN-msCib2-IRES-GFP | This paper | N/A |
| pCAGEN-msCib3-IRES-GFP | This paper | N/A |
| pCAGEN-msCib2-E64D-IRES-GFP | This paper | N/A |
| pCAGEN-msCib2-R66W-IRES-GFP | This paper | N/A |
| pCAGEN-msCib2-F91S-IRES-GFP | This paper | N/A |
| pCAGEN-msCib2-C99W-IRES-GFP | This paper | N/A |
| pCAGEN-msCib2-I123T-IRES-GFP | This paper | N/A |
| pCAGEN-msCib2-R186W-IRES-GFP | This paper | N/A |

| REAGENT or RESOURCE | SOURCE | IDENTIFIER |
|---|---|---|
| pCAGEN-msCib2-N68Q-IRES-GFP | This paper | N/A |
| pCAGEN-msCib2-I114F-IRES-GFP | This paper | N/A |
| pCAGEN-msCib2-T131L-IRES-GFP | This paper | N/A |
| pCAGEN-msCib2-V152F-IRES-GFP | This paper | N/A |
| pET28a-huCIB3 | This paper | N/A |
| pET28a-huCIB3-E150QK151H | This paper | N/A |
| pET15b-msTmc1(298-352aa) | This paper | N/A |
| pN3-MYC-msTmc1-D100-105 | This paper | N/A |
| pN3-MYC-msTmc1-D108-111 | This paper | N/A |
| pN3-MYC-msTmc1-D114-121 | This paper | N/A |
| pN3-MYC-msTmc1-D125-129 | This paper | N/A |
| pN3-MYC-msTmc1-D298-303 | This paper | N/A |
| pN3-MYC-msTmc1-D305-307 | This paper | N/A |
| pN3-MYC-msTmc1-D309-312 | This paper | N/A |
| pN3-MYC-msTmc1-D316-319 | This paper | N/A |
| pN3-MYC-msTmc1-D323-329 | This paper | N/A |
| pN3-MYC-msTmc1-D336-339 | This paper | N/A |
| pN3-MYC-msTmc1-D340-344 | This paper | N/A |
| pN3-MYC-msTmc1-D349-352 | This paper | N/A |
| pN3-MYC-msTmc1-M105106A | This paper | N/A |
| pN3-MYC-msTmc1-M109110111A | This paper | N/A |
| pN3-MYC-msTmc1-M120122A | This paper | N/A |
| pN3-MYC-msTmc1-M305306307A | This paper | N/A |
| pN3-MYC-msTmc1-M309310311A | This paper | N/A |
| pN3-MYC-msTmc1-M315316317318A | This paper | N/A |
| pN3-MYC-msTmc1-M326327328329A | This paper | N/A |
| pN3-MYC-msTmc1-M336337338A | This paper | N/A |
| pN3-MYC-msTmc1-M340341342343344A | This paper | N/A |
| pN3-MYC-msTmc1-1-181 | This paper | N/A |
| pN3-MYC-msTmc1-1-210 | This paper | N/A |
| pN3-MYC-msTmc1-1-396 | This paper | N/A |
| pN3-MYC-msTmc1-1-757 | This paper | N/A |
| pN3-MYC-msTmc1-71-396 | This paper | N/A |
| pN3-MYC-msTmc1-81-396 | This paper | N/A |
| pN3-MYC-msTmc1-91-396 | This paper | N/A |
| pN3-MYC-msTmc1-100-396 | This paper | N/A |
| pN3-MYC-msTmc1-127-396 | This paper | N/A |
| pN3-MYC-msTmc1-1-375 | This paper | N/A |
| pN3-MYC-msTmc1-D130-134 | This paper | N/A |

| REAGENT or RESOURCE | SOURCE | IDENTIFIER |
|---|---|---|
| pN3-MYC-msTmc1-D136-141 | This paper | N/A |
| pN3-MYC-msTmc1-D141-143 | This paper | N/A |
| pN3-MYC-msTmc1-D145-147 | This paper | N/A |
| pN3-MYC-msTmc1-D154-158 | This paper | N/A |
| pN3-MYC-msTmc1-D161-165 | This paper | N/A |
| pN3-MYC-msTmc1-D171-175 | This paper | N/A |
| pN3-MYC-msTmc1-D176-181 | This paper | N/A |
| pN3-MYC-msTmc1-D182-186 | This paper | N/A |
| pN3-MYC-msTmc1-D187-190 | This paper | N/A |
| pN3-MYC-msTmc1-D289-294 | This paper | N/A |
| pN3-MYC-msTmc1-D295-297 | This paper | N/A |
| pN3-MYC-msTmc1-D289-300 | This paper | N/A |
| pN3-MYC-msTmc1-D298-303 | This paper | N/A |
| pN3-MYC-msTmc1-F312R | This paper | N/A |
| pN3-MYC-msTmc1-W315D | This paper | N/A |
| pN3-MYC-msTmc1-Y317A | This paper | N/A |
| pN3-MYC-msTmc1-N321K | This paper | N/A |
| pN3-MYC-msTmc1-E323K | This paper | N/A |
| pN3-MYC-msTmc1-I332D | This paper | N/A |
| pN3-MYC-msTmc1-F336D | This paper | N/A |
| pN3-MYC-msTmc1-K337Q | This paper | N/A |
| Software and Algorithms | | |
| Deltavision Elite Software (SoftWoRx Resolve 3D) | GE | https://www.gelifesciences.com/en/ee/shop/deltavision-elite-high-resolution-microscope-p-04420 |
| Imaris 9.1 | Oxford Instruments | https://imaris.oxinst.com/packages |
| Igor pro 7 | WaveMetrics | https://www.wavemetrics.com/ |
| TDT System 3 | Tucker-Davis Technology | https://www.tdt.com/products/ |
| ER-10C Low Noise™ DPOAE Microphone | Etymotic Research | https://www.etymotic.com/auditory-research/microphones/er-10c.html |
| MATLAB | Mathworks | https://www.mathworks.com/products/matlab.html |
| Origin Pro 7.5 | Origin Lab | https://www.originlab.com/ |
| Graph-Pad Prism 6 | Graph Pad Software | https://www.graphpad.com/scientific-software/prism/ |
| ImageJ | Schneider et al., 2012 | https://imagej.nih.gov/ij/index.html |
| Patchmaster 2.35 | HEKA | http://www.heka.com/downloads/downloads_main.html |
| Micro-Manager 1.4 software. | Edelstein et al., 2010 | https://micro-manager.org/wiki/ |
| Adobe Illustrator 2020 | Adobe | https://www.adobe.com/ |
| Adobe Photoshop 2020 | Adobe | https://www.adobe.com/ |
| XDS | Kabsch, 2010 | http://xds.mpimf-heidelberg.mpg.de |

| REAGENT or RESOURCE | SOURCE | IDENTIFIER |
|---|---|---|
| AIMLESS | Evans and Murshudov, 2013 | http://www.ccp4.ac.uk |
| Phenix | Adams et al., 2004 | http://www.hkl-xray.com/ |
| Coot | Emsley and Cowtan, 2004 | https://www2.mrc-lmb.cam.ac.uk/personal/pemsley/coot/ |
| Pymol | Schrödinger | https://pymol.org/2/ |
| PDBePISA | Krissinel and Henrick, 2007 | http://www.ebi.ac.uk/pdbe/pisa/ |